Tectonophysics 744 (2018) 155–176

Contents lists available at ScienceDirect

Tectonophysics

journal homepage: www.elsevier.com/locate/tecto

Thermal history of the central part of the Karst Dinarides, Croatia: Combined application of clay mineralogy and low-T thermochronology

Jan Środoń[a], Aneta A. Anczkiewicz[a,*], István Dunkl[b], Igor Vlahović[c], Ivo Velić[d], Bruno Tomljenović[c], Tadeusz Kawiak[a], Michał Banaś[a], Hilmar von Eynatten[b]

[a] Institute of Geological Sciences, Polish Academy of Sciences, Research Centre in Kraków, Senacka St. 1, PL-31002 Kraków, Poland
[b] Sedimentology and Environmental Geology, Geoscience Center, University of Göttingen, Goldschmidtstrasse 3, D-37077 Göttingen, Germany
[c] University of Zagreb, Faculty of Mining, Geology and Petroleum Engineering, Pierottijeva 6, HR-10000 Zagreb, Croatia
[d] Geolog d.o.o. and Croatian Geological Summer School, Pančićeva 5, HR-10000 Zagreb, Croatia

ARTICLE INFO

Keywords:
AFT and (U–Th–Sm)/He thermochronology
Burial clay diagenesis
Burial diagenesis of haematite
Karst Dinarides
Thermal history

ABSTRACT

This study was undertaken to obtain the first thermochronological and clay mineralogy data to unravel the thermal history (maximum temperatures, timing, origin of the temperature increase, rate of exhumation) of the central part of the Karst Dinarides, exposed along the NE Adriatic coast in the Velebit Mt. and neighbouring areas. An additional research objective was tracing the behaviour of haematite crystals during diagenesis. The lower, partly clastic part of the sedimentary section (Upper Carboniferous to Triassic), covered by a thick succession of Mesozoic carbonates has been studied by a combination of mineralogical techniques (XRD + SEM), K–Ar dating of illite, apatite fission track (AFT), as well as apatite and zircon (U–Th–Sm)/He thermochronology.

A consistent model of the thermal history of the study area was obtained. The Carboniferous to Triassic sequences SW of the Split–Karlovac Fault experienced maximum burial temperatures between 200 and 270 °C, while lower palaeotemperatures (ca. 150 °C) were detected in the Middle Triassic rocks to the NE of the fault. The maximum palaeotemperatures were recorded earlier (during the Late Cretaceous–Palaeocene) than expected during the period of maximum sedimentary and/or tectonic burial in Middle Eocene and Early Oligocene, corresponding to the major thrusting phase in the studied part of the Dinarides. Rapid exhumation started in the studied structural domains between 80 and 35 Ma, i.e. between the Campanian and the end of Eocene, followed in some domains by a younger exhumation and cooling pulse.

Haematite, the main carrier of the palaeomagnetic signal in the studied area, was shown to recrystallize at temperatures above 120 °C, which explains the appearance of secondary magnetization well below the Curie point of haematite, such as reported recently in the Central Velebit Mt. area.

1. Introduction

The central part of Karst Dinarides, well exposed along the NE Adriatic coast in the Velebit Mt. and neighbouring areas, belongs to the Dinaric–Hellenic orogenic system, which formed by thin-skinned Eocene–Oligocene thrusting along the eastern Adria Microplate margin (e.g. Blašković, 1988; Herak, 1991; Tari-Kovačić and Mrinjek, 1994; Tari, 2002; Schmid et al., 2008; Korbar, 2009). This thrusting involved several thousand metres of mostly shallow-marine upper Palaeozoic and Mesozoic carbonates and siliciclastics. The thrusting followed the Late Cretaceous–earliest Palaeogene closure of the Neotethys Ocean along the Sava Suture Zone of the Internal Dinarides (e.g. Pamić, 2002; Schmid et al., 2008; Ustaszewski et al., 2010).

The sedimentary history and tectonics of the Karst Dinarides have been extensively studied since 1960s (Vlahović et al., 2005, 2012 and references therein). However, in contrast to other circum-Mediterranean orogens, where thermochronologic data are abundant and extensively used in reconstruction of thermal histories of lithostratigraphic, structural or tectonic units, such data are lacking from the Karst Dinarides, thus leaving the questions on thermal history (about level, timing, and origin of maximum palaeotemperatures, rates of exhumation, etc.) still open. Addressing these questions is complicated by predominantly pure carbonate lithology, which excludes the use of organic geochemistry, commonly applied in such studies. This methodological challenge inspired our study and we used a rare combination of methods (XRD and K–Ar dating of clay minerals, apatite fission track (AFT) as well as apatite and zircon (U–Th–Sm)/He thermochronology) in order to reconstruct thermal history of the area. The study also

* Corresponding author.
E-mail address: ndstruzi@cyf-kr.edu.pl (A.A. Anczkiewicz).

https://doi.org/10.1016/j.tecto.2018.06.016
Received 4 July 2017; Received in revised form 23 May 2018; Accepted 21 June 2018
Available online 25 June 2018
0040-1951/

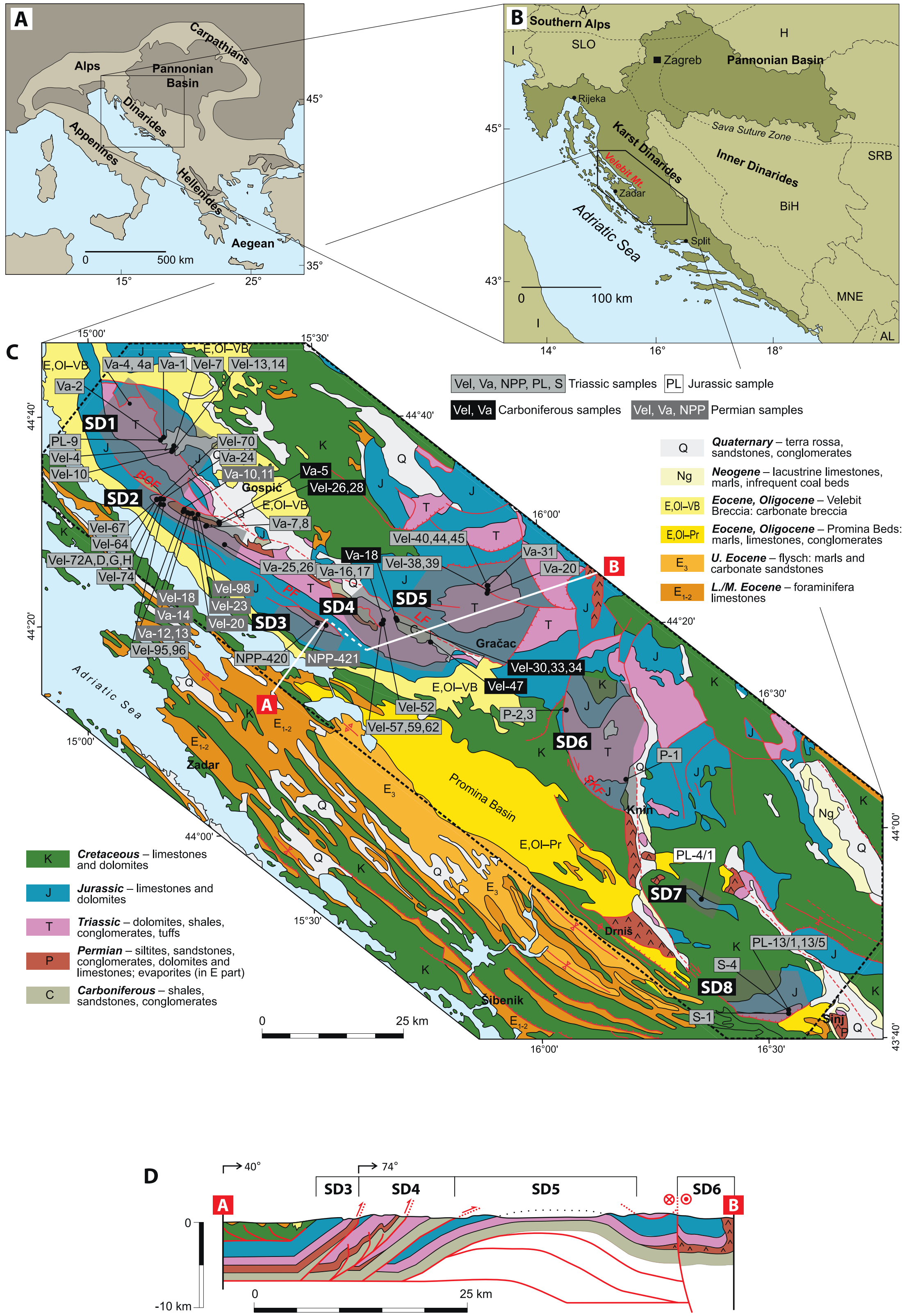

Fig. 1. Location of the study area (A and B) and sample locations with respect to the eight structural domains discussed in the text (SD1 to SD8) and marked by grey fields on the geological map of the central part of the Karst Dinarides (C, simplified after FGI, 1970) and schematic geological profile (D) showing SW-dipping thrusts of a passive roof duplex system formed above the Bruvno anticline (SD5), which accommodated top-to-NE displacement (simplified after Tomljenović et al., 2017). Major faults: BOF – Brušane–Oštarije Fault; PF – Paklenica Fault; LF – Lika Fault; SKF – Split–Karlovac Fault.

addressed interest of the oil industry regarding thermal history of the area, and the need to explain the nature of diagenetic remagnetization of haematite, detected by the parallel palaeomagnetic study (Werner et al., 2015).

2. Geological setting

The study area is located in the central part of the Karst Dinarides of Croatia, extending from the NW along the Velebit Mt. to the Sinj area in the hinterland of Split in the SE (Fig. 1). The Dinarides, a mountain chain connecting the Southern Alps with the Albanides/Hellenides (Fig. 1A), are generally subdivided into the Karst Dinarides (mostly corresponding to the External or Outer Dinarides) extending along the NE Adriatic coast, and the Inner Dinarides located between the Karst Dinarides and the Pannonian Basin to the NE (Fig. 1B). For more information on the palaeogeographical evolution of the ancient Adriatic Carbonate Platform and its underlying and overlying deposits which formed Karst Dinarides see Vlahović et al. (2005) and references therein.

2.1. Sedimentary succession of the study area

The studied part of Karst Dinarides is composed of several thousand metres of mostly shallow-marine late Palaeozoic and Mesozoic carbonates, including several intervals of the Upper Carboniferous to Middle Triassic siliciclastics. Synsedimentary tectonics in the late Palaeozoic, Middle Triassic, Early and Late Jurassic and Late Cretaceous resulted in significant differences in thickness of sedimentary succession. This succession is covered by Cenozoic carbonate and siliciclastic deposits, the latter of Middle Eocene to Oligocene age, accumulated during the major compressional tectonic phase in this part of the Dinarides (Fig. 1C). The Carboniferous, Permian and Triassic siliciclastic intervals, as well as one Jurassic interval were the subject of this study.

The Upper Carboniferous succession is locally > 500 m thick, characterized by predominance of sandstones (quartz and lithic graywackes) and dark shales with intercalations of fossiliferous limestones and quartz conglomerates (Ivanović et al., 1976; Sokač et al., 1976a). The Lower Permian clastic succession is composed of 250–500 m thick alternation of reddish sandstones, siltstones and shales with intercalations of quartz and conglomerates with lithic clasts and rare limestone lenses (Ramovš et al., 1990; Aljinović et al., 2008). These are followed by locally > 900 m thick succession of Middle to Upper Permian dolomites with limestone intercalations (Fio et al., 2010 and references therein). The conformably overlying 400 to > 800 m thick Lower Triassic deposits are mostly composed of mica-bearing sandstones, siltstones and shales, frequently interbedded with carbonates. The Middle Triassic rocks were deposited in lagoonal environments, characterized by thick limestones with tuff and sandstone intercalations, and in small intraplatform basins with prevailing shales, sandstones, tuffs and cherts. The tectonic segmentation resulted in highly variable thicknesses (150–1400 m) of the Middle Triassic deposits. The period between the Middle and the Late Triassic (mostly late Rhaetian) was characterized by local emergence that resulted in the deposition of 0–120 m thick succession of reddish to greenish sandstones, siltstones, shales and conglomerates with tuffs (including bentonite layers) and locally bauxites (Ivanović et al., 1976; Sokač et al., 1976a, 1976b).

The carbonate deposition commenced already in the Carboniferous (Sremac, 2012; Japundžić and Sremac, 2016) and the proportion of carbonates increased significantly in the Late Permian and Triassic. The major amount of carbonates accumulated during the Jurassic and Cretaceous on the semi-isolated Adriatic Carbonate Platform (Vlahović et al., 2005). In the study area the Jurassic and Cretaceous carbonate sequence is 3000 to 4000 m thick. This massive carbonate deposition ended at different stages of the Late Cretaceous, when the platform became gently deformed, disintegrated and mostly emerged, partly due to SW–NE compression (see e.g. Marinčić, 1997). Predominantly clastic carbonate deposition during the middle Eocene–early Oligocene was controlled by SW-directed propagation of thrusting and formation of foredeep to piggy back basin(s) (Promina Basin on Fig. 1C; e.g. see Vlahović et al., 2012). The thickness of Cenozoic deposits is highly variable depending on their position within a complex array of mostly tectonically controlled depositional environments, and complete thickness of carbonate and clastic sequences in the Promina Basin area may reach couple of thousands of metres (Ivanović et al., 1973).

2.2. Cenozoic tectonics of the Karst Dinarides

As a result of the Cenozoic Adria–Europe convergence, thrusting gradually propagated from internal into more external SW parts of the orogen, as confirmed by the migration of foreland basins that become progressively younger towards SW and SE (Tari, 2002; Schmid et al., 2008; Korbar, 2009; Ustaszewski et al., 2008, 2010). This basin migration is documented by syn-orogenic flysch deposits of the Middle–Upper Eocene (e.g. Babić et al., 2007), Oligocene (e.g. Tari-Kovačić and Mrinjek, 1994; Korbar, 2009) or locally even Miocene age (e.g. de Capoa et al., 1995; Mikes et al., 2008).

According to the GPS data the Adria–Europe convergence is still ongoing with a velocity of 2–5 mm/yr (e.g. Grenerczy et al., 2005; Bennett et al., 2008; Caporali et al., 2009; Weber et al., 2010). In the upper crust this movement is mostly accommodated by thrusting and strike-slip faulting, as indicated by seismicity and fault-plane solution data (e.g. Herak et al., 2005; Benetatos and Kiratzi, 2006; Kastelic and Carafa, 2012; Kastelic et al., 2013; Ustaszewski et al., 2014), supplemented by geomorphic data indicating variable Pleistocene and Holocene uplift and subsidence (e.g. Benac et al., 2008; Faivre et al., 2010; Babić et al., 2012; Surić et al., 2014).

2.3. Sampled structural domains

Samples were collected from eight structural domains (SD1 to SD8) separated by major faults delineated on the geological maps of former Yugoslavia (Fig. 2) and characterized by Palaeozoic–Mesozoic successions different in thickness and/or lithofacies (Fig. 3). The original maximum depositional thicknesses above the sampled intervals (at the end of carbonate platform sedimentation in the Late Cretaceous) were estimated from the Basic Geological Maps, sheets Gospić (Sokač et al., 1974), Udbina (Šušnjar et al., 1973), Obrovac (Ivanović et al., 1973), Knin (Grimani et al., 1972), Drniš (Ivanović et al., 1977), Sinj (Papeš et al., 1982), and our own data.

Structural domains SD1–SD4 belong to the Velebit Mt., which is the most prominent geomorphological unit in the study area, extending for ca. 145 km along the Adriatic coast, with the highest peaks exceeding 1700 m a.s.l. Structurally, this mountain represents a complex assemblage of km-scale NW–SE trending anticlines, exposing Palaeozoic and Triassic rocks in their cores. Almost as a rule, the northeastern anticline limbs are cut and reduced by km-scaled faults, the most of which are interpreted on geological maps with normal, top-to-NE offset, thus presumably overprinting the previously formed anticline structures (e.g. Bahun, 1974). In this work, however, we followed the working hypothesis recently proposed by Tomljenović et al. (2017), which presumes that these faults are SW-dipping thrusts of a passive roof duplex system formed above the Bruvno anticline (SD5) which accommodated top-to-NE displacement (Fig. 1D). In contrast to the NE limbs, the SW limbs of anticlines are well preserved as homoclines composed of moderately to steeply SW-dipping Palaeozoic–Cenozoic strata. Above the upper Palaeozoic and Triassic sequences, they expose the complete Jurassic carbonate platform sequence conformably overlain by Cretaceous and Lower–Middle Eocene carbonates (the latter known as the Foraminifera limestones). Jurassic and partly Cretaceous deposits are in contact with Palaeogene–Neogene(?) carbonate breccia (the Jelar Deposits of Bahun, 1963, or the Velebit Breccia of Vlahović et al., 2012), cropping out along the SW slope of the mountain (Fig. 1).

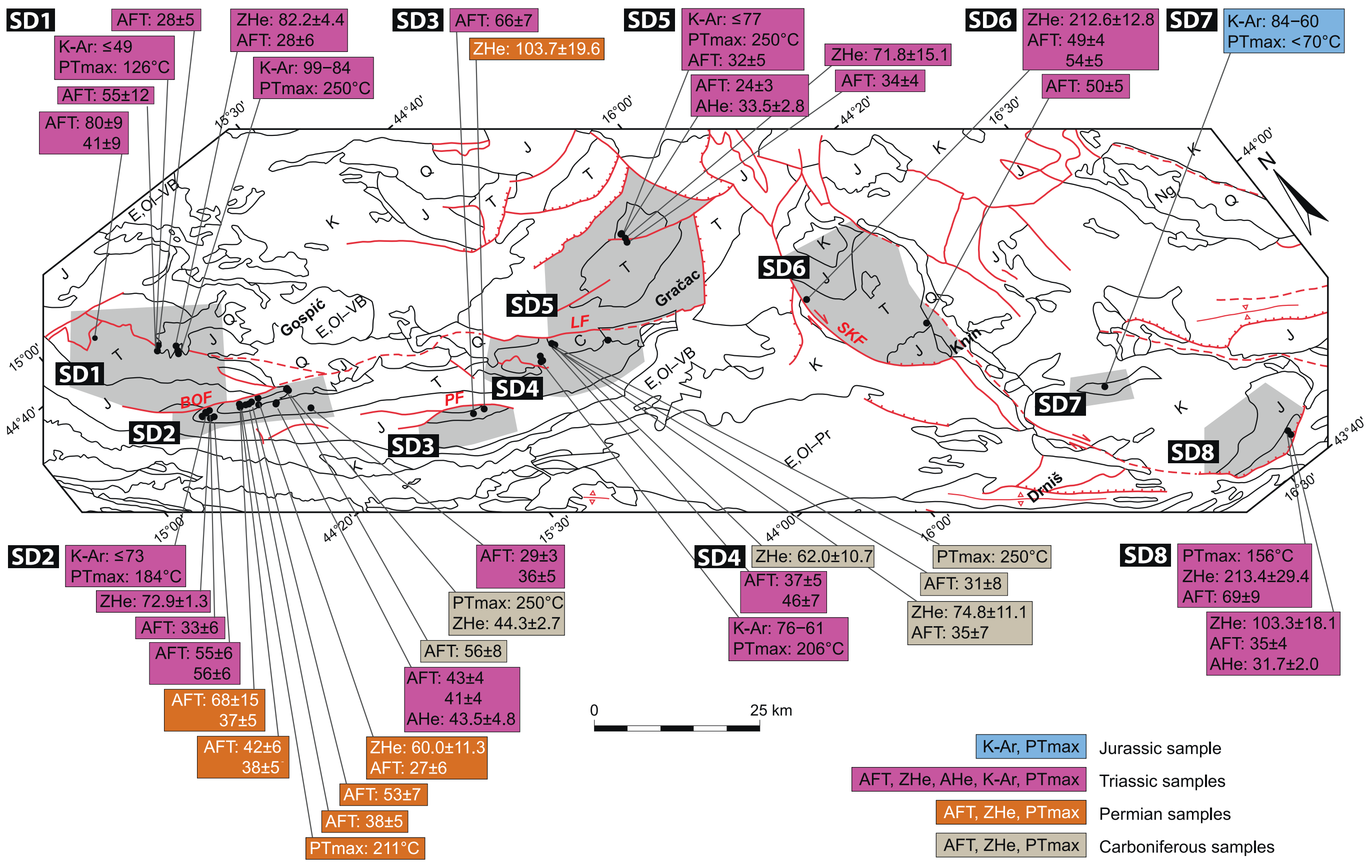

Fig. 2. Distribution of measured K–Ar, AFT, ZHe, and AHe ages and the maximum palaeotemperatures as evaluated from illite–smectite geothermometer, plotted on the simplified geological map of the central part of the Karst Dinarides. Grey areas indicate the structural domains SD1 to SD8. Major faults: BOF – Brušane–Oštarije Fault; PF – Paklenica Fault; LF – Lika Fault; SKF – Split–Karlovac Fault.

Structural domain SD1 (Donje Pazarište) represents a SW-dipping homocline in the NW part of the Velebit Mt., which is on the surface composed of the Triassic and Jurassic rocks, separated from the neighbouring SD2 domain by the Brušane–Oštarije Fault. SD1 is characterized by thick Ladinian deposits of a relatively deep and short-lived intraplatform basin.

Structural domain SD2 (Baške Oštarije–Brušane) is an anticline exposing the Carboniferous to Jurassic strata with typical Dinaric strike (NW–SE), reduced to the NE by the Brušane–Oštarije Fault and separated from SD3 by the reverse Paklenica Fault. This domain is characterized by a complete lack of the Ladinian deposits, indicating that the Middle–Late Triassic emergence started there earlier than in most of other domains.

Structural domain SD3 (Paklenica) represents a SW-dipping

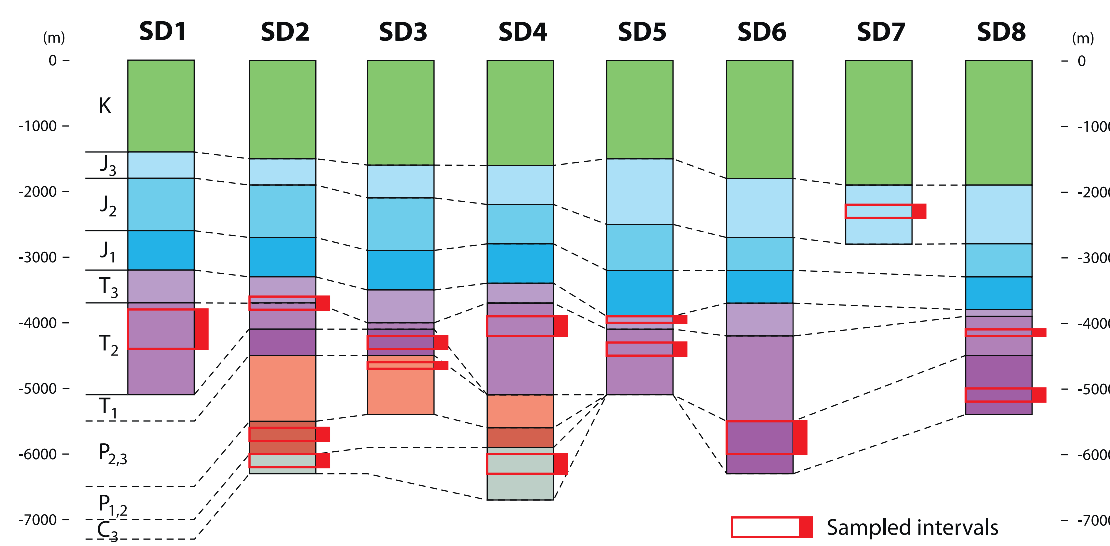

Fig. 3. Stratigraphic columns of the eight investigated structural domains at the end of the major phase of the carbonate platform sedimentation, reconstructed from the available geological data. The vertical scale in metres. Sample intervals marked in red. (For interpretation of the references to color in this figure legend, the reader is referred to the web version of this article.)

homocline composed of the Permian, Triassic, Jurassic and Cretaceous succession, lithostratigraphically very similar to the SD2 domain. It is bounded to the NE by the Paklenica thrust Fault that brought this domain into structural position above the SD2 and SD4 domains.

Structural domain SD4 (Sveti Rok–Ričica) represents the structural continuation of SD2 towards SE, being composed of the Carboniferous and Permian rocks in the cores of the NW–SE striking anticlines, which are reduced to the NE by SW-dipping thrust faults. However, unlike the SD2 and SD3 domains where the Ladinian deposits are lacking due to the longer stratigraphic hiatus, this domain is characterized by gradual thickening of the Ladinian deposits towards the SE.

Structural domain SD5 (Bruvno) represents a faulted dome-like to brachyanticline structure gently elongated in the ENE–WSW direction for ca. 25 km and separated along its SW limb from SD4 by the Lika Fault (Ivanović et al., 1973; Šušnjar et al., 1973; Sokač et al., 1974). To the N, NE and SE this structure is overthrusted by thrust sheet(s) that put the Lower Triassic clastic rocks on top of Jurassic carbonates of the Bruvno structure. SD5 is characterized by a specific sedimentary succession compared to all other studied domains, since the Permian and Lower Triassic deposits are there completely lacking due to the very long stratigraphic hiatus. Therefore, during the latest Palaeozoic and the earliest Triassic, this domain was probably uplifted with respect to neighbouring domains.

Structural domains SD6–SD8 are located NE of the Split–Karlovac Fault (Chorowicz, 1975), which according to the palaeogeographical reconstructions by Chorowicz (1977) had a precursor that was periodically separating deeper environments eastwards (including evaporites in the Late Permian; e.g. Dedić et al., 2018) from shallower environments SW of the fault (e.g. during the Late Permian–Early Triassic, Late Triassic, Jurassic and latest Cretaceous), and thus would be characterized by a normal top-to-E sense of slip. However, today that fault is usually considered as a major dextral transpressive zone in this part of the Dinarides during the Eocene–Oligocene and Neogene (e.g. Schmid et al., 2008).

Structural domain SD6 (Poštak–Knin) is characterized by intensely folded Triassic, Jurassic and Lower Cretaceous sequences, composing a nappe that is thrusted on top of the structural unit exposed in the Plavno tectonic window (Grimani et al., 1972). This domain is separated from SD5 by the dextral Split–Karlovac Fault.

Structural domain SD7 (Svilaja East) represents a NW–SE striking anticline composed of the Jurassic carbonates in the core and the Cretaceous carbonates in the limbs. It is separated from SD6 by the NW–SE striking dextral fault, which is considered as a splay of the dextral Split–Karlovac Fault.

Structural domain SD8 (Svilaja West) represents the NW-dipping limb of the NE–SW striking fault-related anticline formed in the hanging wall of the NW-dipping thrust considered as a frontal ramp of the dextral Split–Karlovac Fault. This anticline limb exposes the Lower and Middle Triassic succession of siliciclastic deposits associated with the Middle Triassic tuffs that gradually pass into the Jurassic and Cretaceous carbonates of the SD7 domain.

3. Samples and methods

Sampling was focused on three stratigraphic levels with siliciclastic rocks (including pyroclastics) suitable for the applied methods: Upper Carboniferous, Lower Permian and Lower to Middle/Upper Triassic, and an additional Jurassic sample. Fig. 2 and Table S1 show the locations of 101 shale, pyroclastic and sandstone samples, collected from natural outcrops and road cuts. The clay mineralogical studies were performed on shales and pyroclastics, while fission track and (U–Th–Sm)/He thermochronology were done on apatite and zircon crystals separated from the pyroclastic and sandstone samples.

The applied mineralogical methods include: mineral identification by XRD, XRD quantification of the bulk rock mineral composition from random preparations using Rietveld-based AUTOQUAN program (Bergmann and Kleeberg, 1998), which was found most appropriate for the quantification of illite polytype mixtures, separation of < 0.2 μm fraction using Jackson techniques (Jackson, 1975), identification of clay minerals, the measurement of smectite percent (% S) in mixed-layer illite–smectite from the XRD patterns of oriented, glycolated preparations of < 0.2 μm fractions, and scanning electron microscopy (SEM) of selected samples using an instrument equipped with EDS.

The percentage of smectite layers (% S) in illite–smectite present along with discrete illite was evaluated from the peak positions in 5–9° 2θ and 31–35° 2θ range (Środoń, 1984), using the experimental regressions developed from the data of Środoń et al. (2009a). If both numbers were measurable, their average was used as the final estimate of % S with precision of ± 2%. If these peaks were absent or too diffuse to be measured, % S was classified as 0 if air-dry and glycolated patterns were the same or almost the same, or as < 5 if the difference was significant. For pure illite–smectites, % S was also evaluated from the peaks in 15–18° 2θ and 26–27° 2θ ranges, using the experimental regressions developed from the data of Środoń et al. (2009a) and all four numbers were averaged. Selected clay subfractions, separated by flow-through high-speed centrifugation, were dated by the K–Ar method. Details of these techniques can be found in Środoń et al. (2013).

Apatite and zircon crystals were separated using standard crushing, sieving, magnetic and heavy liquids techniques. Single-crystal grains were dated by the (U–Th–Sm)/He method, usually 3 grains per sample. The crystals were selected very carefully; only fissure-free specimens were used, with well-defined completely convex external morphology; euhedral crystals were preferred. The shape parameters were determined and archived by multiple digital photomicrographs. The crystals were wrapped in platinum capsules of ca. 1 × 1 mm size. The Pt capsules were heated up by an infra-red laser and the extracted gas was purified using a SAES Ti–Zr getter at 450 °C. The chemically inert noble gases and a minor amount of other rest gases were then expanded into a Hiden triple-filter quadrupole mass spectrometer equipped with a positive ion counting detector. Crystals were checked for degassing of He by sequential reheating and He measurement. The residual gas is usually around 1 to 2% after the first extraction in case of zircon crystals and always below 1% in case of apatite crystals. Following degassing, samples were retrieved from the gas extraction line and spiked with calibrated ^{230}Th and ^{233}U solutions. Zircon crystals were dissolved in pressurized teflon bombs using a mixture of double distilled 48% HF and 65% HNO_3 at 220 °C during five days. Apatite crystals were dissolved in pre-spiked 2% HNO_3. The 0.4 ml solutions were analysed by isotope dilution using a Perkin Elmer Elan DRC II ICP-MS with an APEX micro-flow nebulizer. Sm, Pt and Ca were determined by external calibration. The ejection correction factors (F_t) were determined for the single crystals by a modified algorithm of Farley et al. (1996) using an in-house spreadsheet. Effective uranium (eU) was calculated with the formula (eU) = (U) + 0.24 × (Th) + 0.008 × (Sm) (Leprêtre et al., 2017).

Apatite fission-track thermochronology was performed by the external detector method (Gleadow and Duddy, 1981; Gleadow et al., 1983; Gleadow et al., 2002). The external detector method and the ζ age calibration approach were used to determine the fission-track ages (Gleadow, 1981; Hurford and Green, 1983; Hurford, 1990a, 1990b). Polished grain mounts were etched for 20 s in 5 N HNO_3 at 20 °C. The standard glass CN5 was used as a dosimeter to monitor the neutron flux. Thin flakes of low-U muscovite were used as external detectors. Samples together with age standards (Fish Canyon, Durango, and Mount Dromedary apatites) and CN5 standard glass dosimeters were irradiated with thermal neutron nominal flux of $9\text{x}10^{15}$n/cm^2 at the Oregon State University TRIGA reactor in the USA. After the irradiation the muscovite external detectors were etched for about 45 min in 40% HF in order to reveal the induced tracks. The spontaneous and induced tracks were counted by optical microscopy at 1250× magnification using a NIKON Eclipse E-600, equipped with motorised stage, digitising tablet and drawing tube controlled by program FTStage 4.04 (Dumitru, 1993). Data analyses and age calculations based on a Zeta value for CN5 ζ_{CN5} of 348.18 ± 6.52 were calculated using program Trackkey 4.2 (Dunkl, 2002). All quoted AFT ages are "central ages" (Galbraith and Laslett, 1993), and the spread of single grain ages was assessed using the dispersion of the central age and chi-square test (Galbraith, 1981; Green, 1981). In nearly all analysed samples about 20 or more apatite grains were selected for analyses. Only clean, defect- and inclusion-free grains were selected for track counting. The etch pit diameter (Dpar) was used to check annealing kinetics and the composition of apatites (Burtner et al., 1994; Carlson et al., 1999; Barbarand et al., 2003). At least four etch pits (Donelick et al., 2005) per single analysed grain have been measured. The crystals chosen for confined track measurements had a well-polished surface, parallel to the c-axis. For each sample, as many confined track lengths as possible were measured (Gleadow et al., 1986). The measured confined track lengths were corrected for their crystallographic orientation by applying the computer code HeFTy (Donelick et al., 1999; Ketcham et al., 2007a).

The modelling of the thermal history was performed by using HeFTy software (Ketcham, 2005). The program requires input data (such as measured AFT age, track length distribution, kinetic parameter as Dpar for apatite and apparent ZHe age, actinide concentration and diameter of the dated crystals) to define "acceptable" time–temperature paths that pass statistical criteria and also conform to a possible set of user-defined geological constraints (Ketcham, 2005). Thermal histories were modelled using the multi-kinetic model (Ketcham et al., 2007b). Randomly generated thermal histories predict the AFT age and length parameters, and compare them to the measured data. An acceptable fit corresponds to thermal histories representing the t–T paths that give a goodness of fit (GOF) value > 0.05 for both the age and the length distribution (Ketcham, 2005). A good fit corresponds to thermal histories with a GOF value > 0.5. For a comprehensive overview of fission-track methods and their modelling techniques, see Donelick et al. (2005), Ketcham (2005), and Ketcham et al. (2007b).

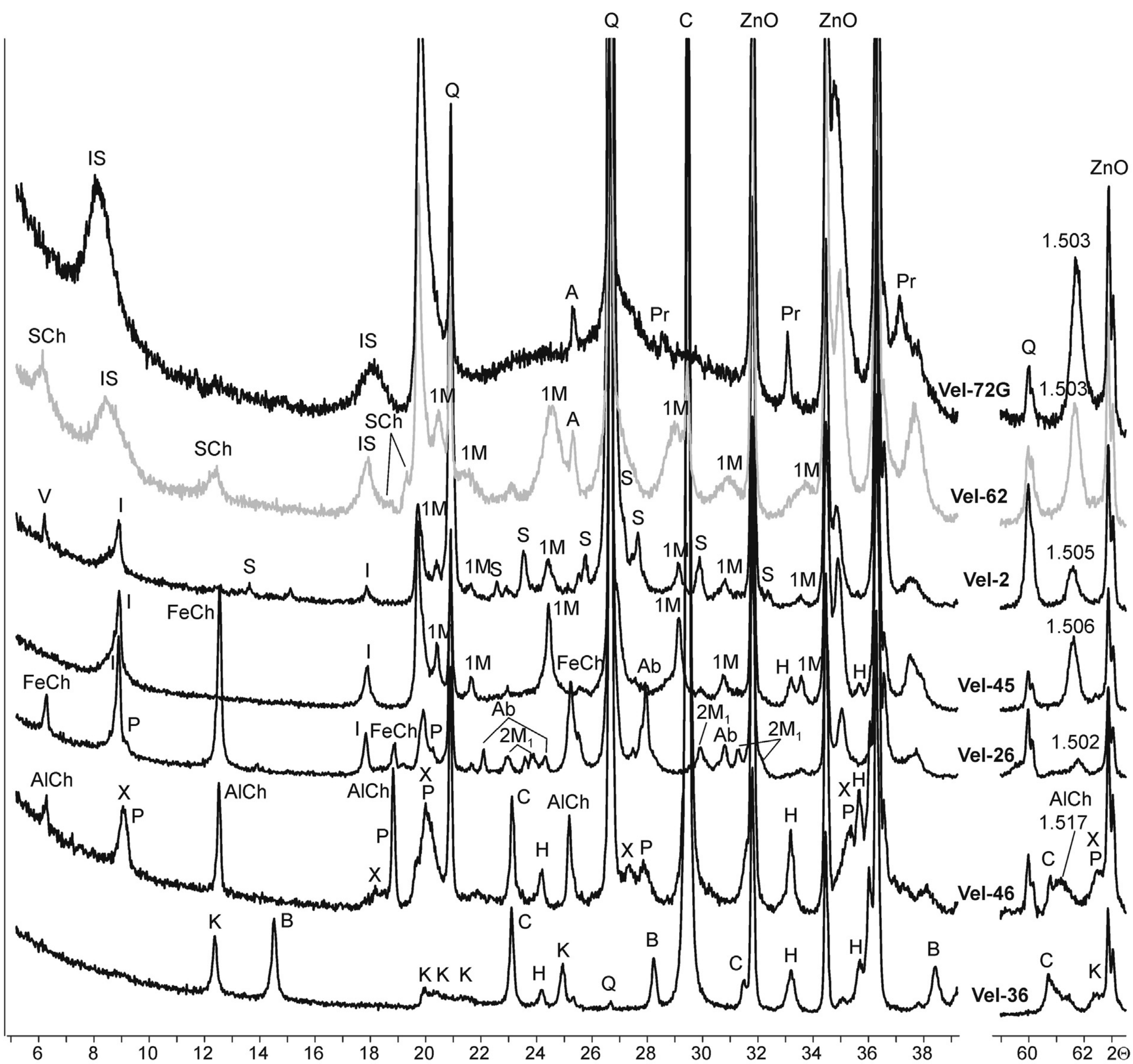

Fig. 4. Selected XRD patterns of the bulk rock random preparations, illustrating the mineralogical variability encountered in the studied samples. IS – illite–smectite, Q – quartz, A – anatase, Pr – pyrite, C – calcite, ZnO – internal standard, SCh – swelling chlorite, 1M – $1M_{tv}$ polytype (IS or illite), V – vermiculite, I – illite, S – sanidine, H – haematite, FeCh – Fe-chlorite, P – paragonite, Ab – albite, $2M_1$ – $2M_1$ polytype of illite, AlCh – Al-chlorite, X – a phase intermediate between paragonite and illite, K – kaolinite, B – boehmite. Numbers are d_{060} of 2:1 minerals (Å).

4. Experimental results

4.1. Bulk rock mineral composition

The commonly occurring minerals, detected by XRD in the pelitic and pyroclastic samples are quartz, albite, K-feldspar, illite, mixed-layer illite–smectite, chlorite, kaolinite, calcite, dolomite, pyrite, haematite, and goethite (Table S2). A few samples contain vermiculite, paragonite, siderite, jarosite, and gypsum; boehmite, and marcasite were found in one sample each. Fig. 4 presents characteristic XRD patterns and indicates the peaks diagnostic for different minerals. Biotite was identified by EDS SEM.

K-feldspar was found to occur as two varieties: sanidine/orthoclase in Kalinovača (SD1), and adularia, accompanied by albite in Vršina (SD4), both within Ladinian tuffs.

Pure illite occurs as $2M_1$ or 1M variety, and illite–smectite as 1M or 1Md. Some samples contain pure polytypes and other samples their mixtures (Table S3). Stratigraphic control over polytype distribution is observed: 1M polytype is characteristic of the Ladinian pyroclastics in Kalinovača (SD1), Vršina (SD4) and Bruvno (SD5), while pure 1Md polytype is characteristic of the Upper Triassic rocks in Baške Oštarije (SD2). Permian and Carboniferous rocks contain $2M_1$ or $2M_1$ + 1Md polytypes. Polytypes differ by the *060* values (Table S3): 1.500–1.502 Å are characteristic of the Carboniferous, Permian and Lower Triassic $2M_1$ illites, while Middle/Upper Triassic 1M and 1Md illites have 1.503–1.507 Å values, indicative of higher Fe content (Heuser et al., 2013).

Polytype 1M is characteristic of more illitic compositions of illite–smectite (< 10% S) than polytype 1Md (> 10% S). Crystal morphologies of both polytypes look similar in SEM: thin plates ca. 1 μm in diameter. Among 1M polytype samples, those from Kalinovača (SD1) and Bruvno (SD5) are essentially pure illites and very perfect trans-vacant varieties (Vel-2 and 45 in Fig. 4). 1M polytype illites from Vršina (SD4) are slightly more expandable and are mixed trans-vacant/cis-vacant varieties, as evidenced by peak broadening and displacement (Vel-62 in Fig. 4; cf. Moore and Reynolds, 1997). d_{001} of illites vary from 9.96 Å for $2M_1$ varieties to 9.92 Å for some 1M and 1Md samples (Table S3). The latter, lower values indicate aluminoceladonitic composition, up to 50% (Środoń et al., 2013).

Most chlorites are non-swelling, iron-rich varieties (even *00l* peaks are stronger: Vel-26 from SD2; Fig. 4). In two samples, from Permian and Triassic, Al-chlorites were identified, based on relative intensities of basal reflections (*003* peak strongest: Vel-46 from SD5; Figs. 4 and 5), in both cases together with paragonite (Table S3). d_{001} = 14.16–14.17 Å (based on *002*, *003* and *004*) indicates di-trioctahedral chlorite sudoite (Lin and Bailey, 1985), which is consistent with d_{060} = 1.517 Å and the chemical composition, relatively rich in Mg (Fig. 6A). Sudoite occurs as isometric plates, of ca. 1.5–2 μm diameter (Fig. 6B).

Two samples contain swelling chlorite (Vel-52 and Vel-62 from SD4; see Fig. 4: broadened and displaced reflections) and two samples (Vel-1 and Vel-2, SD1) contain vermiculite (strong *001* reflection with d_{001} bigger than chlorites and very weak higher orders: Fig. 4). Swelling chlorite and vermiculite are considered to be the products of contemporary weathering of chlorite at outcrops (cf. Środoń et al., 2013; Marynowski et al., 2017).

Kaolinite, if present in abundance, can be identified as ordered variety by the peaks in 20–22° 2θ range (e.g. Vel-36, SD5; Fig. 4). In a

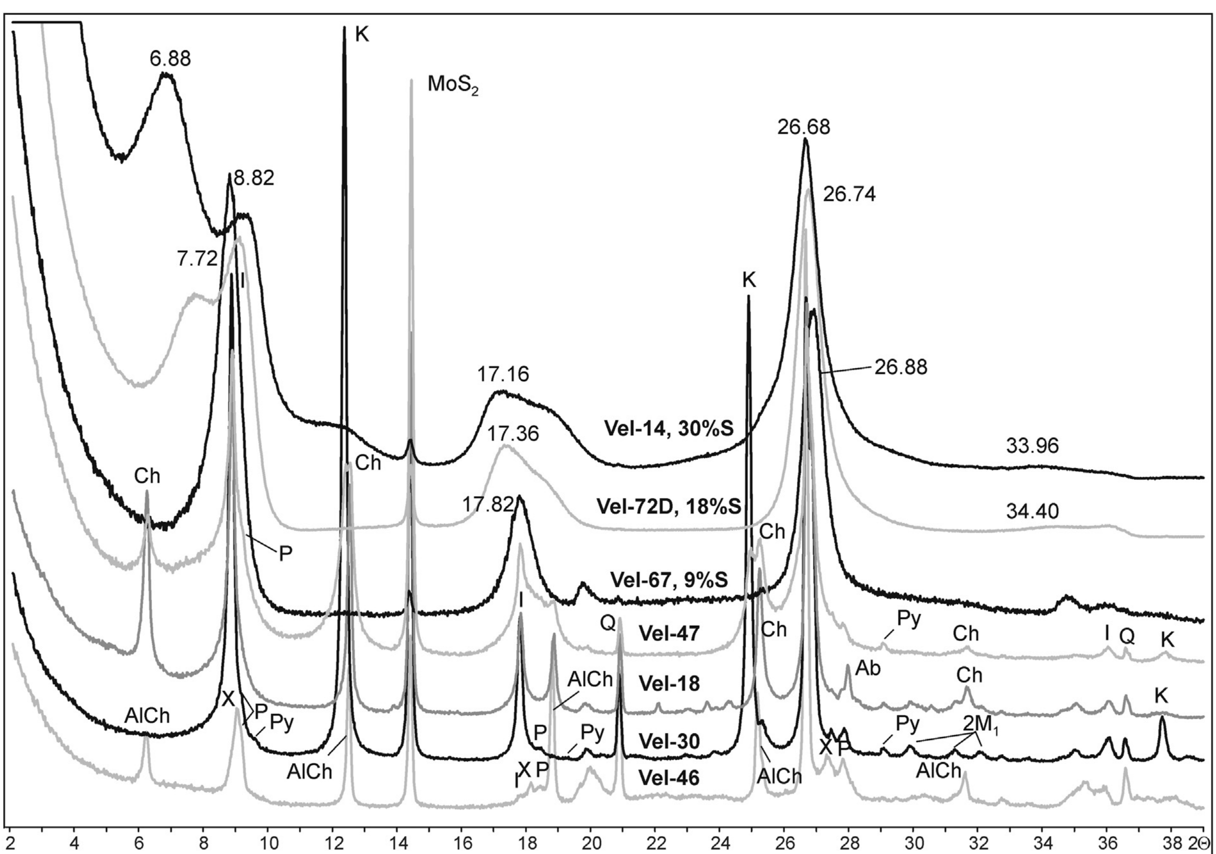

Fig. 5. Selected XRD patterns of the oriented, glycolated preparations of < 0.2 μm fractions, illustrating the mineralogical variability encountered in the studied samples. Numbers are 2θ positions of illite–smectite basal reflections, used for the measurements of percent smectite, listed by the sample name. Ch – chlorite, AlCh – Al-chlorite, X – a phase intermediate between paragonite and illite, P – paragonite, Py – pyrophyllite, K – kaolinite, MoS_2 – synthetic molybdenite internal standard, Q – quartz, Ab – albite, $2M_1$ – hkl reflections of $2M_1$illite.

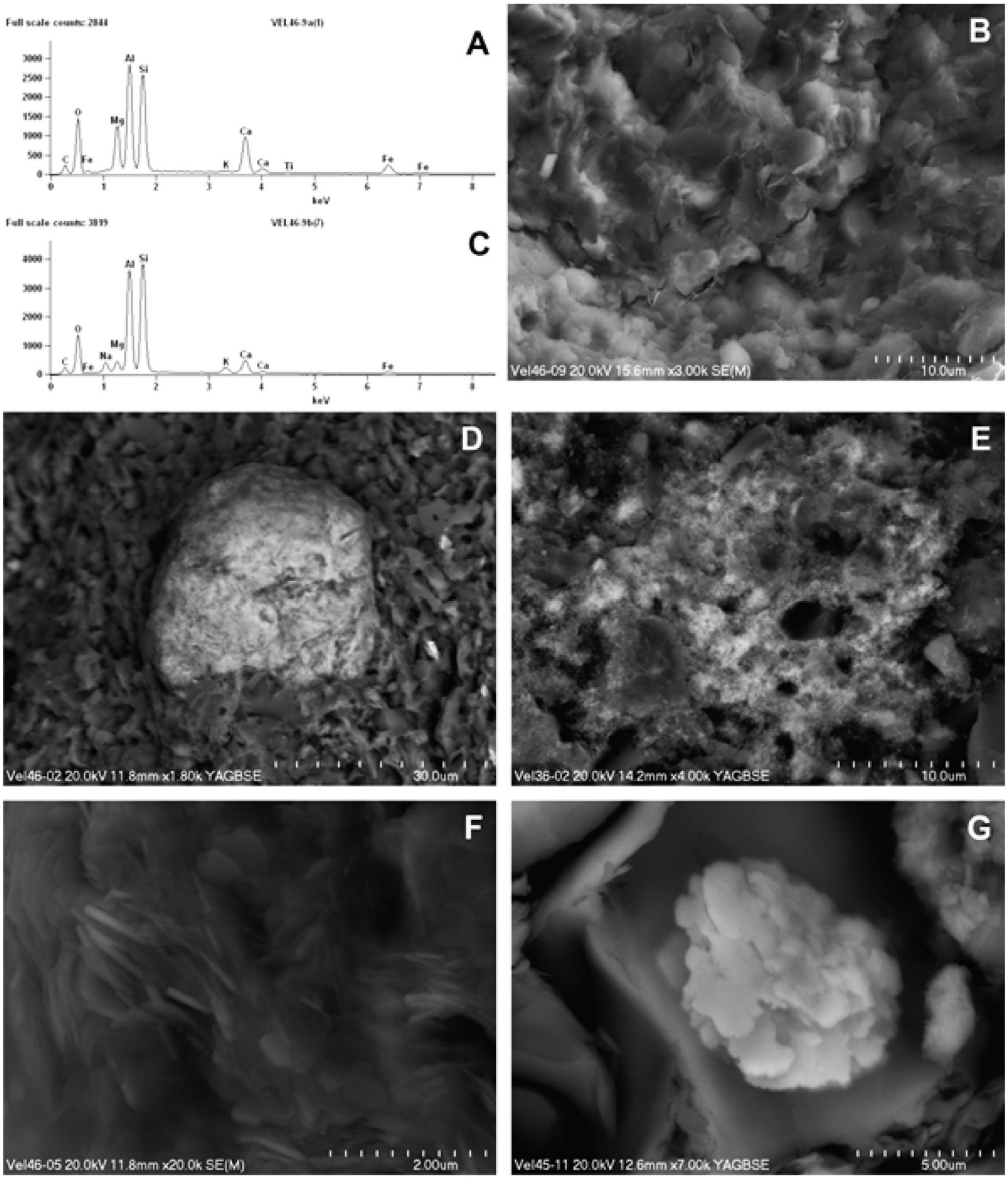

Fig. 6. SEM photos and EDS data for selected minerals: A – chemical composition of Al-chlorite sudoite (Vel-46); B – crystals of sudoite and other clays in Vel-46; C – chemical composition of aggregate of paragonite and other 2:1 minerals in Vel-46; D and E – aggregates of haematite (BSE mode); F – detailed view of typical haematite crystals; G – unusually large haematite crystals in altered pyroclastic grain (Vel-45).

Triassic sample from Kalinovača (Vel-10, SD1) an admixture of mixed-layer kaolinite–smectite was identified, both by *00l* reflections and in the *060* range.

Paragonite is present in several $2M_1$ illite-rich Carboniferous samples only in trace amounts, in one case together with trace amount of pyrophyllite along with dominant kaolinite (Vel-30, SD4; Fig. 5). In the Triassic sample Vel-46 (SD5), rich in calcite and Al-chlorite, paragonite is abundant and accompanied by a mixed-layer micaceous phase (X in Fig. 5), and traces of illite. Based on *002*, *003* and *005* reflections, paragonite in this sample has d_{001} = 9.63 Å, close to the end-member variety and free of potassium in the interlayers (cf. Fig. 146a in Fleet, 2003). The mineral X has d_{001} = 9.76–9.78 Å (based on *002*, *003* and *005* reflections), intermediate between K and Na varieties. The 2:1 minerals occur as sub-micron flakes (Fig. 6B), so definitely they are clay-sized. The high Na content was confirmed by EDS (Fig. 6C).

Haematite is identified as relatively well-crystallized, because its *104* reflection at 2.703 Å is sharp (Vel-36 and 46, SD5; Fig. 4), not much broader than *110* reflection at 2.519 Å (cf. Brindley and Brown, 1980, their Fig. 6.3). Commonly, haematite is observed by BSE as aggregates, up to tens of microns in diameter, rounded (Fig. 6D) or more loose (Fig. 6E), composed of sub-micron plates (Fig. 6F). Their TiO_2/Fe_2O_3 ratio (from EDS) is low: 0.02–0.09. Exceptionally large, micron-size haematite crystals were observed as alteration products of an illitized pyroclastic grain (Fig. 6G).

Boehmite was identified only in one Ladinian sample (Vel-36, SD5; Fig. 4), classified as bauxite based on its pisolithic texture. Boehmite is of sub-micron size, accompanied by kaolinite, calcite, and haematite.

Biotite was spotted by SEM in sample Vel-45 (SD5) as 200 μm long crystals in a groundmass composed of micron-size illite crystals. Other volcanogenic grains, except of unaltered large crystals of quartz, are illitized and contain accumulations of haematite.

The quantitative XRD data (Table S2) reveal exceptionally low

Table 1
Results of K–Ar measurements obtained on different grain-size fractions.

Sample, Str. Dom.	Site, stratigraphic age	Fraction	% K_2O	% $^{40}Ar^*$	$^{40}Ar^*$ [pmol/g]	Age [Ma]	Error [Ma]
PL-9, SD1	Donje Pazarište	< 0.2	4.65	21.483	332.02	49	4
	Ladinian (230–235 Ma)	2–0.2	2.89	24.676	261.665	62	4
Vel-10, SD1	Kalinovača	< 0.02	4.08	25.035	596.173	99	5
	Ladinian (230–235 Ma)	0.02–0.05	3.29	28.219	439.863	91	4
		0.05–0.2	3.18	42.243	392.221	84	3
Vel-72G, SD2	Baške Oštarije	< 0.02	7	40.756	748.687	73	1
	Carnian (225–230 Ma)	0.02–0.05	7.1	54.139	847.455	81	1
		0.05–0.2	6.99	63.274	965.345	93	1
Vel-26, SD2	Brušane	< 0.2	3.94	75.098	1423.542	235	2
	Carboniferous (286–360 Ma)	2–0.2	4.06	63.91	1313.187	212	3
Vel-57, SD4	Vršina	< 0.02	8.13	47.377	903.844	76	1
	Ladinian (230–235 Ma)	0.02–0.05	8	45.426	711.695	61	1
		0.05–0.2	8.01	38.738	719.781	61	1
Vel-30, SD4	Pilar	< 0.2	3.93	41.113	1241.594	207	3
	Carboniferous (286–360 Ma)	2–0.2	4.06	73.245	1327.872	214	2
Vel-45, SD5	Bruvno	< 0.02	8.12	39.247	919.94	77	1
	Carnian (225–230 Ma)	0.02–0.05	7.99	89.192	2148.857	178	1
		0.05–0.2	7.79	85.915	1601.333	137	1
PL-4/1, SD7	Maovice	< 0.2	1.66	39.19	204.961	84	3
	Kimmeridgian (152–156 Ma)	2–0.2	1.71	30.987	149.156	60	4

quartz contents in Triassic bentonites from Baške Oštarije (SD2) and Vršina (SD4). Potassium feldspars are more abundant only in some tuffs from Kalinovača (SD1) and Vršina (SD4), and in a Lower Triassic micaceous shale from Baške Oštarije (SD2). Albite is more common and present in variable amounts: from 0 to 20%. Calcite does not exceed a few percent in the Carboniferous and Permian rocks, but varies over a broad range (0–65%) in the Triassic rocks. Dolomite distribution is opposite: < 1% in the Triassic, but occasionally up to 25% in the Carboniferous and Permian. Siderite was detected only in the Carboniferous of Pilar (SD4). Elevated pyrite contents (up to 5%) characterize the centre of a thick bentonite bed in Baške Oštarije (SD2) and blue shale from the same profile, which contains also marcasite. Haematite contents reach 5% in some Permian and Triassic samples. Goethite, gypsum and jarosite are minor components (< 2%), detected only in the Triassic rocks from Kalinovača (SD1) and Baške Oštarije (SD2).

Among clay minerals the illite/illite–smectite group is by far the most abundant, generally in the 25–55% range in the Carboniferous and Permian and 25–90% in the Triassic samples. Kaolinite reaches 15% in the Carboniferous and Permian rocks. In the Triassic samples kaolinite is almost absent, with a few exceptions for Ladinian samples: two from Kalinovača (SD1) and a bauxite sample from Vrace (SD4), which contain also boehmite and dominant calcite. Chlorite is less abundant than kaolinite, most common in the Carboniferous and Permian samples (up to 9%).

If average numbers are used (Table S2) six major clear trends in mineral composition controlled by stratigraphy appear: in the Triassic rocks quartz, dolomite, kaolinite, and chlorite are less abundant, while illite + illite–smectite and calcite are more abundant. There are no major differences, so it can be concluded that on average the investigated sections have quite similar mineral composition.

4.2. Illite–smectite composition

The samples selected for clay fraction separation represent both shales and pyroclastics. The samples contain only illite or illite–smectite, or most often mixtures of these components and other clay minerals (examples of XRD patterns in Fig. 5). The measured % S varies from 0 to 30% S with one exception for the Kimmeridgian clay from Maovice (SD7), which contains an illite–smectite with 79% S (Table S3).

These results were used as reference in the measurement of % S directly from the bulk rock XRD patterns of the samples without illite (pyroclastics) or where the low-angle illite–smectite peak was clearly separated from the 10 Å illite (e.g. Vel-72G from SD2 and Vel-62 from SD4; Fig. 4). The position of the low-angle peak was used for quantification by applying the regression for illite–smectites in air-dry Ca form, developed from the data of Środoń et al. (2009a). The bulk rock and the < 0.2 μm measurements show excellent agreement (Table S3).

4.3. K–Ar ages of illite

Detrital illite contamination is the most serious problem in dating authigenic illite growth. XRD is the best technique available for screening samples for K–Ar dating (e.g. Środoń et al., 2002). The samples identified by XRD as containing illite–smectite free of discrete illite contamination (pure pyroclastics) were preferably used for K–Ar dating. Such samples were not available in the Carboniferous section, thus regular shales were dated. Multiple measurements were made for each sample: either 2–0.2 μm and < 0.2 μm fractions, or 0.2–0.05 μm, 0.05–0.02 μm, and < 0.02 μm fractions were dated (Table S1). All K–Ar ages are younger than the stratigraphic ages. The ages of illite fractions from the Jurassic rocks are Late Cretaceous to Palaeocene (84–60 Ma), those from Triassic rocks are Jurassic/Early Cretaceous to Palaeocene/Early Eocene (178–49 Ma), and the illites from the Carboniferous rocks yield Triassic K–Ar ages (235–207 Ma; Table 1).

4.4. Zircon (U–Th–Sm)/He ages

General zircon (U–Th–Sm)/He results are presented in Table 2 and Fig. 2. For this regional study, where remarkable differences were detected between the tectonic units, the averaged sample ages seem to be the conventional and the most pragmatic way to present the areal distribution of the low-T ages. The mean ages determined in 11 Palaeozoic and Mesozoic samples range from 213 to 44 Ma, with the majority clustering between 83 and 60 Ma. Reproducibility of replicates is good for the majority of samples; most replicates reproducing within two sigma error. In the map view an increase of the ZHe ages in the southeastern structural domains is observed (SD6, SD8, Table 2). In the Donje Pazarište and Baške Oštarije–Brušane domains in the NW part of the Velebit Mt. (SD1 and SD2, respectively) ZHe ages of 83–60 Ma were determined, with one exception showing 44 Ma (sample Vel-28 from SD2 along the Permian–Carboniferous boundary). In the Sveti Rok–-Ričica area (SD4) the ZHe ages are around 75–62 Ma, in the Carboniferous rocks, and in the Bruvno area (SD5) a mean age of 72 Ma was determined in the Triassic rocks. In the area of Paklenica (SD3), the ZHe

Table 2

Apatite and zircon (U–Th–Sm)/He data. Amount of helium is given in nano-cubic-cm in standard temperature and pressure. Amounts of radioactive elements are given in nanograms. Ejection correct. (F_t): correction factor for alpha-ejection (according to Farley et al., 1996 and Hourigan et al., 2005). Uncertainties of helium and the radioactive element contents are given as 1 sigma, in relative error %. Uncertainty of the single grain age is given as 2 sigma in Ma and it includes both the analytical uncertainty and the estimated uncertainty of the F_t. Uncertainty of the sample average ages are in 1 standard error, as $(SD)/(n)^{1/2}$; where SD = standard deviation of the age replicates and n = number of age determinations. eU has been calculated with the formula [eU] = [U] + 0.24 × [Th] + 0.008 × [Sm].

Sample str. dom.	Strat. age	Aliq.	He		U238			Th232			Th/U	Sm			Ejection	*Uncorr.*	Ft-Corr.		eU (ppm)	Sample unweighted aver.	
			Vol.	1s	Mass	1s	Conc.	Mass	1s	Conc.		Mass	1s	Conc.	Correct.	*He-age*	He-age	2s	eU = U + 0.24 × Th + 0.008 × Sm		
			[ncc]	[%]	[ng]	[%]	[ppm]	[ng]	[%]	[ppm]	Ratio	[ng]	[%]	[ppm]	(Ft)	*[Ma]*	[Ma]	[Ma]		[Ma]	1 se [Ma]
Zircon (U–Th)/He ages																					
Vel-7	Ladinian	#1	23.87	1.7	2.829	1.8	313	1.720	2.4	190	0.61	0.060	5	7	0.79	*60.8*	76.5	5.90	358.7	82.2	4.4
SD1		#2	41.10	1.6	4.997	1.8	793	2.135	2.4	339	0.43	0.070	5	10	0.78	*61.6*	79.1	6.40	874.4		
		#3	28.95	1.7	2.855	1.8	276	1.671	2.4	161	0.59	0.050	5	5	0.81	*73.4*	90.9	6.70	314.7		
Vel-74	Triassic	#1	14.05	1.7	1.905	1.8	318	0.806	2.4	134	0.42	0.030	7	5	0.77	*55.3*	72.0	6.00	350.2	72.9	1.3
SD2		#2	29.43	1.7	3.864	1.8	695	1.627	2.4	292	0.42	0.050	6	8	0.77	*57.1*	73.8	6.00	765.1		
Vel-98	L. Permian	#1	4.07	0.9	1.185	1.8	604	0.029	2.6	15	0.02	0.000	35	1	0.69	*28.3*	40.9	4.10	607.6	60	11.3
SD2		#2	2.71	0.9	0.393	1.8	304	0.082	2.4	63	0.21	0.010	17	5	0.68	*54.2*	79.9	8.30	319.2		
		#3	3.13	0.9	0.537	1.8	209	0.283	2.4	110	0.53	0.030	11	10	0.72	*42.7*	59.2	5.40	235.5		
Vel-28	Carboniferous/	#1	8.32	1.7	2.193	1.8	730	0.437	2.4	146	0.2	0.020	7	8	0.73	*29.9*	41.1	3.90	765.1	44.3	2.7
SD	Permian	#2	3.39	1.8	0.731	1.8	251	0.194	2.4	67	0.27	0.010	11	3	0.73	*36.1*	49.6	4.70	267.1		
		#3	7.00	1.7	1.830	1.8	565	0.269	2.4	83	0.15	0.020	9	5	0.72	*30.5*	42.2	4.00	585.0		
NPP-421	U. Permian	#1	3.87	1.2	0.618	1.8	579	0.123	2.4	115	0.2	0.010	22	5	0.68	*49.3*	72.4	7.50	606.6	103.7	19.6
SD3		#2	3.30	1.2	0.378	1.8	321	0.138	2.4	118	0.37	0.010	20	7	0.67	*66.1*	99.1	10.70	349.4		
		#3	4.02	1.2	0.315	1.9	379	0.189	2.4	227	0.6	0.010	21	7	0.66	*91.8*	139.6	15.40	433.5		
Va-18	Carboniferous	#1	6.62	0.9	1.121	1.8	590	0.600	2.4	316	0.54	0.050	8	25	0.7	*43.3*	62.0	6.10	666.0	62	10.7
SD4		#2	6.26	0.9	0.735	1.8	435	0.882	2.4	522	1.2	0.310	5	186	0.68	*54.6*	80.5	8.30	561.8		
		#3	2.09	1	0.508	1.8	276	0.201	2.4	109	0.4	0.080	6	45	0.72	*31*	43.4	4.10	302.5		
Vel-34	Carboniferous	#1	17.60	0.8	3.192	1.8	544	0.615	2.4	105	0.19	0.110	5	19	0.78	*43.5*	55.7	4.20	569.4	74.8	11.1
SD4		#2	17.98	0.8	1.804	1.8	223	0.665	2.4	82	0.37	0.030	9	3	0.8	*75.4*	94.0	6.50	242.7		
		#3	18.02	0.8	2.389	1.8	538	0.771	2.4	174	0.32	0.060	6	13	0.78	*57.8*	74.5	5.70	579.9		
Vel-39	Ladinian	#1	14.41	1.7	2.078	1.8	505	0.252	2.4	61	0.12	0.030	6	6	0.76	*55.6*	73.3	6.40	519.7	71.8	15.1
SD5		#2	5.99	1.7	1.186	1.8	223	0.318	2.4	60	0.27	0.020	8	4	0.87	*39.2*	44.9	2.70	237.4		
		#3	3.96	1.8	0.348	1.9	119	0.177	2.4	60	0.51	0.010	11	3	0.86	*83.5*	97.2	6.20	133.4		
P-2	L. Triassic	#1	5.37	0.9	0.304	1.9	375	0.112	2.4	138	0.37	0.010	22	8	0.7	*133.1*	190.8	18.80	408.2	212.6	12.8
SD6		#2	5.70	0.9	0.320	1.9	320	0.038	2.5	37	0.12	0.000	36	2	0.67	*141.7*	211.9	22.70	328.9		
		#3	3.18	1	0.166	2	225	0.012	2.9	16	0.07	0.000	70	1	0.65	*153.9*	235.1	26.30	228.8		
S-4	M. Triassic	#1	20.24	0.9	1.177	1.8	161	1.118	2.4	153	0.95	0.020	11	3	0.73	*115.2*	157.3	13.80	197.7	213.4	29.4
SD8		#2	26.53	0.9	0.829	1.8	221	1.310	2.4	349	1.58	0.030	12	7	0.74	*190.2*	256.8	21.80	304.8		
		#3	10.48	0.9	0.409	1.8	193	0.540	2.4	255	1.32	0.010	16	6	0.71	*159.7*	226.1	21.40	254.2		
S-1	L. Triassic	#1	3.20	0.9	0.383	1.8	448	0.041	2.5	48	0.11	0.000	31	3	0.58	*67.1*	116.1	15.40	459.5	103.3	18.1
SD8		#2	1.78	1	0.234	1.9	245	0.048	2.5	50	0.2	0.010	23	7	0.66	*59.7*	90.5	9.90	257.1		
Apatite (U–Th)/He ages																					
Va-7	L. Triassic	#1	0.121	2.2	0.027	2.7	17.4	0.003	5.5	2	0.11	0.170	7.3	109	0.65	*34.3*	52.9	6.6	18.752	43.5	4.8
SD2		#2	0.033	3.3	0.010	6.3	10.7	0.002	6.2	2.5	0.23	0.100	7.9	105	0.66	*24.5*	37.2	6	12.14		
		#3	0.039	3.3	0.012	5	16.2	0.004	5.1	5	0.31	0.130	6.7	178	0.57	*23.1*	40.2	6.7	18.824		
Va-31	Carnian	#1	0.041	2.8	0.009	7.2	13.2	0.022	2.8	33	2.5	0.340	7.1	514	0.54	*20.2*	37.7	6.4	25.232	33.5	2.8
SD5		#2	0.113	2.1	0.030	2.6	16.7	0.063	2.5	35.6	2.13	0.820	6.3	463	0.65	*18.3*	28.2	3.4	28.948		
		#3	0.022	4.1	0.005	12.5	8.9	0.017	3	28.6	3.23	0.230	7.1	403	0.48	*16.6*	34.7	7.4	18.988		
S-1	L. Triassic	#1	0.02	4.3	0.004	15.8	3.4	0.018	2.9	14.3	4.25	0.090	8.8	69	0.65	*18.3*	28.3	5.6	7.384	31.7	2
SD8		#2	0.213	1.7	0.071	2	82	0.013	3.2	15.6	0.19	0.230	7.1	269	0.66	*23.2*	35.1	4	87.896		
		#3	0.14	2	0.050	2.1	62.7	0.017	3	20.8	0.33	0.190	7.8	239	0.66	*20.8*	31.7	3.7	69.604		

age is ca. 103 Ma, which is older than in other parts of the Velebit Mt. and its surroundings (SD1, SD2, SD4 and SD5).

One of the oldest ZHe mean ages of 213 Ma was determined in the Lower Triassic rocks of the Poštak–Knin area (SD6). In the SE part of Svilaja Mt. (SD8) the Lower Triassic rocks (sample S-1) yield ca. 103 Ma and the Middle Triassic rocks (sample S-4) ca. 213 Ma. In yet another two cases where ZHe data from the same domain but from different stratigraphic levels are available, the low-T ages derived from samples at lower stratigraphic position are younger than the ages from samples at higher stratigraphic position: samples S-1 and S-4 (103 vs. 213 Ma) from SD8 and samples Vel-98 and Vel-74 (60 vs. 73 Ma) from SD2. This trend reflects that shallow burial depth and lower temperature caused only partial reset in the higher levels, while in lower stratigraphic position full reset took place and the ZHe data are clearly post-climax ages.

The single-crystal ZHe ages are typically between 80 and 70 Ma (full range is from 257 to 41 Ma), while the actinide content ranges from 133 to 874 ppm eU. No correlation between the ZHe ages and the eU content can be detected.

4.5. Apatite fission track ages

The results of thirty three AFT analyses are presented in Table 3, while their regional distribution is shown in Fig. 2. All AFT ages are younger than the corresponding stratigraphic ages and yield a single population of grain ages as shown by high P (χ^2) values. Central ages range from 80 ± 9 to 24 ± 3 Ma, with the vast majority clustering between 50 and 30 Ma.

Horizontal confined track lengths have been measured in 27 samples (Table 3, Fig. 7). The mean track length varies from 14.4 to 11.9 μm, with the vast majority around 13 μm. Due to the relatively low uranium content only six samples yielded the track numbers > 50 (Va-11, Va-7, Va-8, Va-25, P-1, S-1). Considering samples where the track number is sufficient and the track length > 12.9 μm with narrow distribution (SD < 1.6 except for one sample Va-25) we can assume that they experienced after burial a rather slow cooling through the apatite partial annealing zone (PAZ ~ 60–120 °C; e.g., Gleadow et al., 1986; Green, 1986; Wagner and Van den Haute, 1992; Carlson et al., 1999). All AFT ages plotted against their mean track lengths (Fig. 8) show a classic "3/4 boomerang trend" as defined by Green (1986), representing the progressive overprinting of an older component of tracks by heating in a single dominant palaeothermal event. Older samples (> 60 Ma) have longer mean track lengths; these decrease with decreasing age (60–55 Ma), increase again in samples of 55–30 Ma. This trend may suggest more rapid cooling at 50–30 Ma.

The measured Dpars range from 2.5 to 1.5 μm except one sample (Va4a, Dpar 2.8 μm), indicating that samples have variable annealing kinetics. In general, the AFT ages from individual structural domains show no correlation with Dpar. Some samples from the most north-western structural domain (SD1) yielded highly different apparent AFT ages despite closely situated sampling sites (Va-4 – sandstone and Va-4a – conglomerate; 41 and 80 Ma, respectively). The age difference of this order can be caused by different provenance or highly different chemical composition and annealing characteristics of these apatites

Table 3
Apatite fission track data. Nc – number of crystals; *ρs*, *ρi*, *ρd* – density of spontaneous, induced and detector tracks, respectively ($\times 10^6$ tracks for cm^{-2}); *Ns*, *Ni*, *Nd* – number of counted spontaneous, induced and detector tracks; P (χ^2) – probability obtaining Chi-square value for n degree of freedom (where n = no. crystals-1; Galbraith, 1981; Green, 1981). MTL (μm ± SE) – mean confined track length. SD – standard deviation. Dpar – the etch pit diameter. AFT ages are central ages ± 1σ uncertainty calculated after Galbraith and Laslett (1993). The external detector method and the ζ calibration approach was used to determine the fission tracks age (Gleadow, 1981; Hurford and Green, 1983; Hurford, 1998), with the ζ values of 348.18 ± 6.52 for CN5 glass dosimeters (operator: A.A. Anczkiewicz).

Sample	Str. dom.	Lithology	Nc	Dosimeter		Spontaneous		Induced		P (χ^2)	Central age	MTL ± 1 s.e.	No	SD	Dpar	U
				ρd	*Nd*	*ρs*	*Ns*	*ρi*	*Ni*	[%]	[Ma] ± 1σ	[μm]				[ppm]
Va-4	SD1	Sandstone	12	1.15	3439	0.17	28	0.84	137	99.1	41 ± 9	12.7 ± 0.5	9	1.4	1.9	9.6
Va-4a	SD1	Conglomerate	11	1.27	3825	1.14	143	3.16	395	22.7	80 ± 9	13.6 ± 0.3	39	1.9	2.8	31.3
Va-2	SD1	Sandstone	10	1.18	3558	0.16	27	0.59	100	97.9	55 ± 12	13.2 ± 0.6	10	1.8	2.2	6.9
Va-1	SD1	Sandstone	20	1.16	3472	0.11	32	0.77	229	100.0	28 ± 5	13.4 ± 0.2	46	1.3	2.1	8.8
Vel-7	SD1	Sandstone	8	1.39	4354	0.19	22	1.70	195	99.2	28 ± 6	n.d	n.d.	n.d.	2.0	15.1
Va-24	SD2	Sandstone	15	1.24	3710	0.13	33	0.85	214	100.0	33 ± 6	14.4 ± 0.5	6	1.2	2.2	8.9
Vel-96	SD2	Tuff	18	1.32	4354	0.56	122	2.33	510	100.0	56 ± 6	13.0 ± 0.6	7	1.7	2.3	25.0
Vel-95	SD2	Mudstone	25	1.34	4354	0.43	120	1.87	522	89.6	55 ± 6	13.3 ± 0.4	23	1.7	2.2	17.9
Va-12	SD2	Sandstone	11	1.19	3573	0.27	26	0.83	79	100.0	68 ± 15	11.9 ± 0.6	8	1.7	1.7	9.2
Va-13	SD2	Sandstone	20	1.22	3653	0.22	64	1.24	362	99.6	37 ± 5	13.6 ± 0.2	33	1.3	2.1	13.4
Va-10	SD2	Sandstone	19	1.24	3724	0.27	64	1.36	327	97.7	42 ± 6	12.6 ± 0.4	19	1.6	1.8	13.2
Va-11	SD2	Sandstone	30	1.22	3674	0.27	82	1.50	463	99.6	38 ± 5	12.9 ± 0.2	60	1.3	2.1	14.5
Va-14	SD2	Sandstone	20	1.17	3522	0.35	71	1.87	379	71.5	38 ± 5	12.2 ± 0.3	40	1.9	2.1	20.4
Vel-20	SD2	Sandstone	13	1.27	4354	0.53	85	2.24	359	99.9	53 ± 7	n.d.	n.d	n.d.	2.0	23.9
Vel-98	SD2	Sandstone	15	1.25	4354	0.16	23	1.32	186	100.0	27 ± 6	n.d.	n.d	n.d	2.3	13.2
Va-7	SD2	Tuff	20	1.22	3672	0.40	130	1.99	640	64.6	43 ± 4	13.8 ± 0.2	98	1.5	1.9	19.7
Va-8	SD2	Sandstone	27	1.18	3533	0.41	166	2.06	829	98.5	41 ± 4	13.4 ± 0.2	62	1.5	2.2	21.6
Va-5	SD2	Sandstone	20	1.26	3775	0.26	73	1.01	285	100.0	56 ± 8	12.4 ± 0.4	18	1.7	1.5	9.7
Va-25	SD2	Sandstone	24	1.23	3691	0.18	99	1.32	736	78.8	29 ± 3	14.3 ± 0.2	53	1.6	2.3	14.4
Va-26	SD2	Sandstone	20	1.17	3517	0.26	57	1.47	325	99.6	36 ± 5	13.6 ± 0.6	8	1.8	1.9	15.7
NPP-420	SD3	Sandstone	20	1.16	3470	0.72	149	2.18	450	100.0	66 ± 7	13.2 ± 0.2	40	1.5	2.3	23.2
Va-16	SD4	Sandstone	21	1.25	3768	0.16	62	0.93	367	99.8	37 ± 5	13.9 ± 0.2	48	1.6	2.1	9.0
Va-17	SD4	Sandstone	21	1.26	3787	0.13	62	0.62	298	100.0	46 ± 7	13.6 ± 0.2	46	1.5	2.0	6.9
Vel-33	SD4	Sandstone	10	1.33	4081	0.19	17	1.45	132	98.1	31 ± 8	n.d.	n.d.	n.d.	2.1	13.7
Vel-34	SD4	Sandstone	11	1.37	4354	0.27	34	1.91	237	98.2	35 ± 7	n.d.	n.d.	n.d.	2.2	17.8
Va-20	SD5	Sandstone	20	1.20	3598	0.30	90	1.82	549	90.4	34 ± 4	14.3 ± 0.2	31	1.1	2.0	18.5
Va-31	SD5	Tuff	21	1.23	3699	0.17	73	1.58	661	100.0	24 ± 3	13.8 ± 0.2	38	1.3	2.2	14.3
Vel-44	SD5	Sandstone	20	1.33	4354	0.12	40	0.90	300	100.0	32 ± 5	n.d.	n.d.	n.d.	2.5	8.5
P-2	SD6	Sandstone	21	1.15	3454	0.64	204	2.62	836	57.7	49 ± 4	12.6 ± 0.2	47	1.2	2.2	28.5
P-3	SD6	Sandstone	20	1.18	3548	0.45	163	1.72	621	92.9	54 ± 5	13.0 ± 0.2	42	1.2	2.1	19.7
P-1	SD6	Sandstone	27	1.21	3623	0.34	144	1.49	637	34.6	50 ± 5	13.3 ± 0.2	51	1.5	1.9	14.4
S-4	SD8	Tuff	20	1.12	3376	0.26	78	0.74	220	100.0	69 ± 9	13.3 ± 0.3	24	1.5	2.3	7.6
S-1	SD8	Sandstone	20	1.14	3421	0.42	125	2.38	715	99.7	35 ± 4	13.7 ± 0.2	53	1.4	2.2	25.4

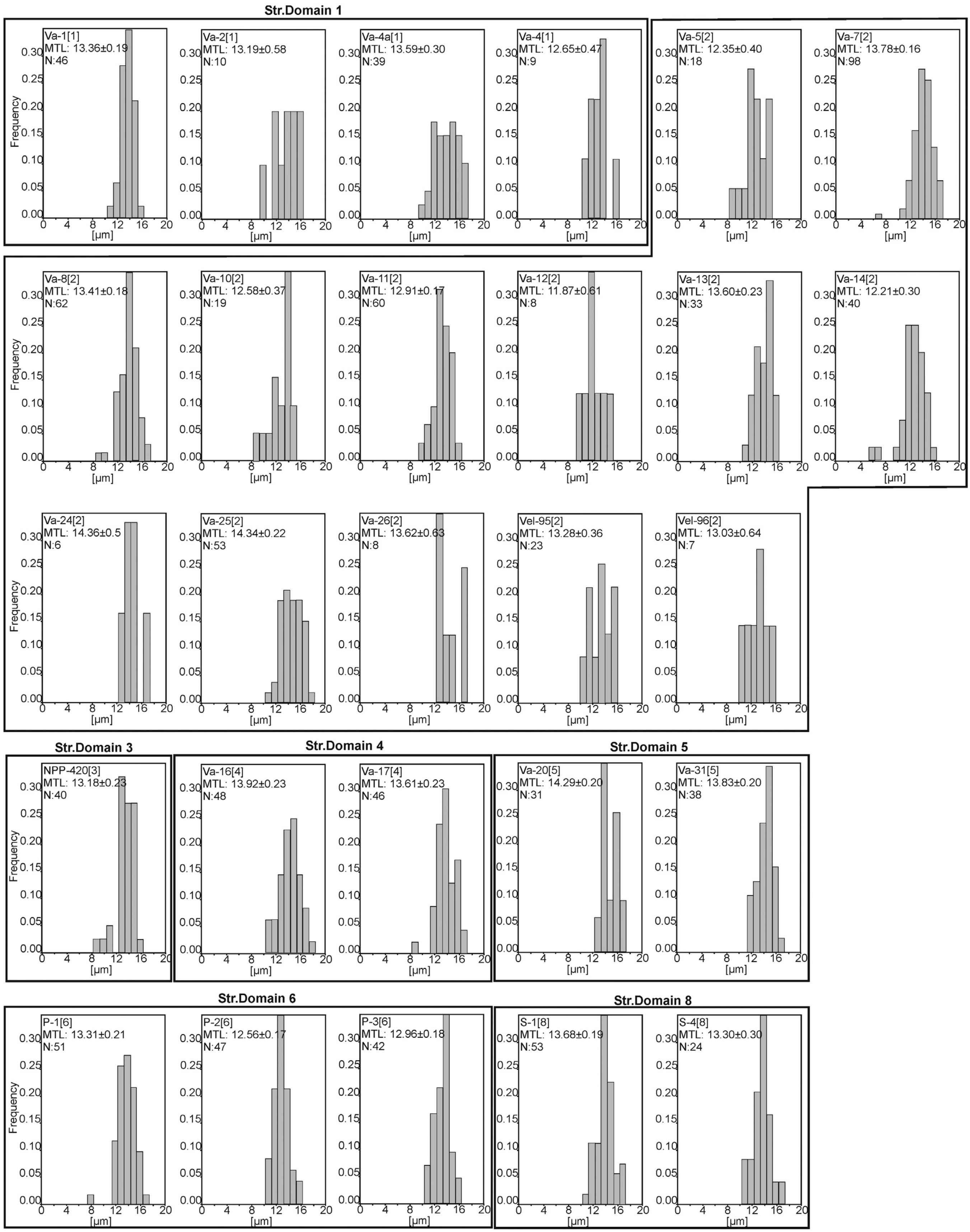

Fig. 7. Length distributions of confined horizontal apatite fission tracks.

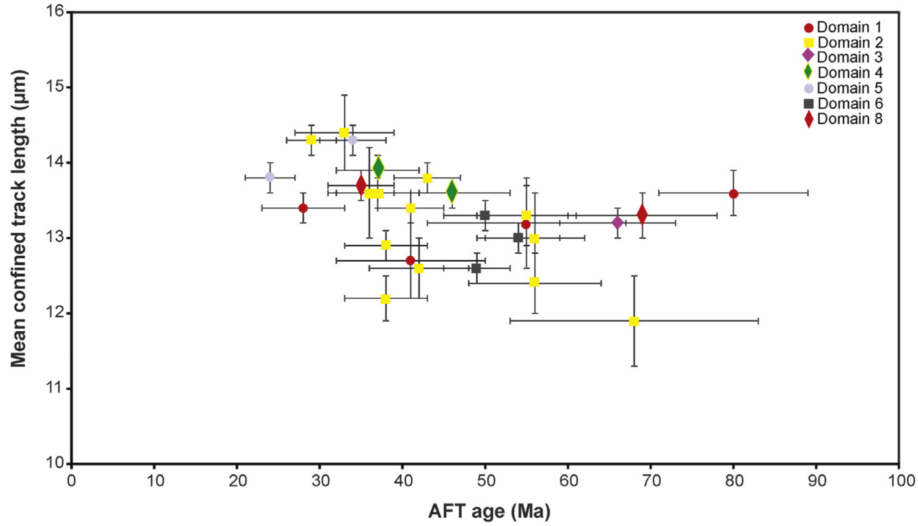

Fig. 8. Mean track length versus AFT ages.

(Barbarand et al., 2003; Burtner et al., 1994; Carlson et al., 1999), which are mirrored in their contrasting Dpar values and track lengths (Table 3).

There is no correlation between the AFT ages and the elevation of the samples in general or within structural units. The AFT apparent ages from the Triassic rocks show more spread in domains SD1 (55–28 Ma), SD2 (56–29 Ma) and SD8 (69–35 Ma) than in domains SD4 (46–37 Ma), SD5 (34–24 Ma) and SD6 (54–49 Ma). AFT age obtained for the Carboniferous rocks from domain SD2 (56 ± 8 Ma) is older than from domain SD4 (35–31 Ma). The Permian rocks in SD2 gave AFT ages between 68 and 27 Ma. Spatial distribution of the AFT data from the Triassic rocks shows older AFT ages (69–66 Ma), which can suggest earlier exhumation, in SD3 and SD8 than in SD5 (34–24 Ma). The spread of AFT ages in SD1 and SD2 (56–28 Ma) suggests the beginning of exhumation in nearly the same time as in domain SD3 and SD8 but which lasted longer.

4.6. Apatite (U–Th–Sm)/He ages

Only three Triassic samples were suitable for apatite (U–Th–Sm)/He thermochronology due to the lack of proper, inclusion-free apatite crystals. The results are shown in Table 2 and Fig. 2; the mean AHe ages range from 43.5 ± 4.8 Ma to 31.7 ± 2.0 Ma. Two of the dated samples (Va-7 from SD3 and S-1 from SD8) are similar within uncertainty to the AFT ages. The AHe age of sample Va-31 from SD5 is much older than the AFT age, which may be caused by poorly visible inclusions due to the rough surfaces of the crystals. This AHe datum was therefore not considered at the evaluation of the thermal history of SD5.

The presented details of AHe results (Tables 2 and 5) from nine single grain AHe ages corrected for alpha ejection showed the age range from 53 ± 7 to 28 ± 3 Ma, with eU contents that range from 7 to 88 ppm and the majority of ages clustering around 30 Ma. No correlation between the AHe ages and the eU content can be detected.

All AFT ages are younger than the corresponding ZHe ages and overlap within uncertainty with the AHe ages (with only one exception: sample Va-31 from SD5 with AFT age of 24 ± 3 Ma and AHe corrected ages in 28.2–37.7 Ma range), which is in agreement with the closure temperatures of these thermochronometers. The latest AHe closure temperature is defined around 50–55 °C (Flowers et al., 2009) and ~70 °C (Gautheron et al., 2009). The closure temperature is linked to the alpha-recoil damage fraction (Shuster et al., 2006; Shuster and Farley, 2009). These models by Flowers et al. (2009) and Gautheron et al. (2009) consider that the recoil damage annealing follows kinetics similar to that for fission tracks, after the results of Ketcham et al. (2007a, 2007b). The damage–annealing rates can be influenced by the apatite chemistry (Gautheron et al., 2013; Djimbi et al., 2015).

5. Discussion of the experimental results

5.1. Estimation of the maximum palaeotemperatures and the palaeogeothermal gradients from illite/smectite ratio

The % S is a good proxy for the maximum palaeotemperature, because smectite illitization is a crystal growth process, which terminates when the maximum palaeotemperatures are reached (Środoń et al., 2000, 2002). Illitization requires the availability of potassium, thus smectite palaeothermometry is directly applicable to rocks with sufficient potassium supply, like shales. The lack of potassium, typical of bentonites, may retard the reaction (e.g. Środoń, 1976, 2007; Altaner et al., 1984; Środoń et al., 2006a). Numerous regional studies applying this approach produced very consistent results (Środoń et al., 2006a, 2006b, 2009b, 2013).

The studied Carboniferous and Permian samples are common shales, but the Triassic samples are often pyroclastics, where serious deficit of potassium may be expected. For such rocks the palaeotemperatures calculated from % S should be regarded as possibly underestimated. All measured % S values are listed in Table S3, but for a given sample area only the minimum values of % S were accepted as representing the maximum palaeotemperatures, which were then calculated (Table S3 and Fig. 2) by applying the calibration of Środoń (2007), based on the present well temperatures in the Miocene/Pliocene section of the East Slovak Basin.

The maximum palaeotemperatures calculated by this approach range from 130 °C to 250 °C for the Carboniferous samples, > 211 °C for the Permian samples, and 126 °C to 250 °C for the Triassic samples. The Jurassic sample from Maovice (SD7) is much less altered, but its pure bentonitic composition does not allow for more accurate palaeotemperature estimation. In general these estimations have to be applied with caution. They are most precise for homogenous detrital lithologies and 60–15% S range. Below 15% S, the precision decreases abruptly because of increased error in % S measurement and slow change of % S with temperature (Środoń, 2007). Pyroclastic lithology and untypical aluminoceladonite composition of 2:1 clay add to the possible error in palaeotemperature estimation by this technique.

5.2. Maximum palaeotemperature estimation from illite polytypes and K–Ar ages

The illite polytype $2M_1$ is characteristic of the anchizone, i.e. the temperature range from 200 to 300 °C. If a sample contains only $2M_1$ polytype (no 1Md or 1M), then theoretically it can be fully detrital, fully authigenic, or a mixture of the two. K–Ar dating may serve as the discrimination criterion: the dates lower than the stratigraphic age indicate either the contribution of authigenic $2M_1$ polytype or rejuvenation of the detrital ages via argon diffusion, which in both cases imply 200–300 °C temperature range (Hunziker et al., 1986). This is the case of the Carboniferous samples Vel-26 and Vel-30, which yield Triassic K–Ar ages (Table 1). The dated < 0.2 μm fraction contains coarse-grained, non-expandable $2M_1$ illite (Vel-26 from SD2, Fig. 4; Vel-30 from SD4, Fig. 5), with the Kübler Index KI = 0.21–0.23, thus indicative of deep anchizone/epizone (e.g. Ferreiro Mählmann, 2001). The Triassic K–Ar age of the Carboniferous samples is older than the Late Cretaceous to Late Palaeocene/Early Eocene K–Ar ages from pure Triassic pyroclastics that were illitized during the same diagenetic event. Such older age indicates the presence of detrital components in the Carboniferous samples, which is consistent with their lithology. The detrital illite has lost a part of its radiogenic argon and/or it is accompanied by authigenic $2M_1$ illite.

5.3. Maximum palaeotemperature estimations from kaolinite, paragonite, and Al-chlorite

In common, potassium-bearing shales kaolinite disappears during diagenesis due to illitization at temperatures between 100 and 150 °C (e.g. Środoń et al., 2006b). In rocks deficient in alkali and alkaline earth cations, however, kaolinite can survive up to 270 °C, when it reacts with quartz to form pyrophyllite (Frey, 1987). The presence of kaolinite and almost complete lack of pyrophyllite in the studied K-depleted pelitic rocks put the upper limit of palaeotemperature at 270 °C.

If the rocks are potassium-deficient but other alkali and alkaline earth cations are available, kaolinite may react to form paragonite and/or brittle micas. These are high-temperature reactions, indicative of the anchizone (Fleet, 2003; Wilson, 2013). Thus the presence of paragonite in the Carboniferous and Triassic samples suggests temperatures > 200 °C.

Al-chlorite is a rare clay mineral, occasionally found in hydrothermal alteration zones, red-beds affected by anchimetamorphic alteration, and pegmatites. It is often associated with kaolinite (Brindley and Brown, 1980; Hillier, 2003; Hillier et al., 2006), but also with pyrophyllite (Biernacka, 2014) and with illite–smectite indicating deep diagenetic grade (Anceau, 1992), which altogether makes a clear temperature estimation difficult. In red-beds of lower grade, tosudite (dioctahedral mixed-layer chlorite–smectite) is often present, but it was not identified in the studied sections. These data combined suggest that Al-chlorite is indicative of deep diagenetic to anchizonal temperatures.

5.4. Maximum palaeotemperature estimations from the XRD characteristics of haematite

Haematite is a common component of continental red-beds, formed during weathering, perhaps originally as hydrated iron oxide (e.g. Środoń et al., 2014). 104 peak broadening data, collected from several locations with different thermal histories (Table 4) indicate that at low diagenetic grade (< 120 °C) the 104 peak is very broad, much broader than the 110 peak, while when the palaeotemperature approaches the anchizone, the width of the 104 and 110 peaks become similar.

These systematic changes indicate that during diagenesis haematite crystals undergo major reorganization. It may involve both the improvement of structural order (Brindley and Brown, 1980) and the crystal growth. Thus the XRD parameters of haematite can be used as a proxy for palaeotemperature. The XRD characteristics of haematite indicate anchimetamorphic alaeotemperatures (Table 4).

5.5. Age of the maximum palaeotemperatures from illite K–Ar geochronology

As authigenic illite–smectite is very fine-grained, the detrital contamination can be detected from K–Ar data if multiple sub-0.2 μm fractions are measured. Such fractions are composed of individual clay crystals, not aggregates, and the detrital components accumulate in coarser fractions, making them look older. Sample Vel-45 is a good example of this case (Table 1).

If a sample contains authigenic illite–smectite free of detrital contamination, the K–Ar ages of different grain-size fractions below 0.2 μm are either similar (fast illitization) or the finest fractions are older than the coarse ones (slow illitization) (Clauer et al., 1997; Środoń et al., 2002).

The slow illitization criterion is met by two Ladinian and one Kimmeridgian bentonite samples Vel-10 (SD1), Vel-57 (SD4), and PL-4/1 (SD7; Table 1). The ages of the finest fractions roughly indicate the beginning of illitization: 99–76 Ma, as they are dominated by thin crystals, generated at the beginning of the illitization process. Coarsest fractions are composed of crystals which grew during the entire illitization process. Consequently, their K–Ar data provide a mixed age within the period of illite growth, which terminates when cooling begins (Środoń et al., 2002). The K–Ar ages of the coarsest fractions of these samples (84 to 60 Ma; Table 1) thus indicate the period of maximum palaeotemperatures, which predates the onset of cooling and/or exhumation. Such spread of K–Ar ages is consistent with the complex and long burial history of the area.

K–Ar ages of two Carnian samples, the bentonite Vel-72G (SD2) and the shale Vel-45 (SD5), indicate weak and strong detrital contamination, respectively (coarse fractions being the oldest). The ages of their finest fractions (73 and 77 Ma, respectively) have to be considered as older than the ages of the maximum burial temperature. Indeed, these ages are within the range obtained from detrital-free samples or, in case of the Ladinian shale sample PL-9 (SD1) even younger (49 Ma). In conclusion, the K–Ar dates of the Triassic samples point to Late Cretaceous or younger ages of the maximum palaeotemperatures. As already discussed in Section 5.2, the Carboniferous samples cannot be used for the age determination.

5.6. Consistency of the clay mineralogical and low-T thermochronological data

The geological interpretation of AFT and (U–Th–Sm)/He data considers the thermal reset of these ages, manifested by the annealing of tracks or the diffusion of He from the crystal lattice. The reset temperatures of ZHe ages are estimated as 170–190 °C (Reiners et al., 2004) or 140–220 °C (Guenthner et al., 2013), but partial reset may take place at lower temperatures ~130–180 °C (Reiners and Brandon, 2006). The closure temperature depends on the time of effective heating and the density of the accumulated radioactive damages (Reiners et al., 2004; Reiners, 2005). The AFT ages reset at 110 ± 10 °C, assuming a cooling rate of 10 °C/Ma (Green and Duddy, 1989) although this temperature varies with the apatite composition (e.g. Cl content; Green et al., 1986; Barbarand et al., 2003) and the annealing kinetics (Green et al., 1986; Ketcham et al., 2007b).

The apatite and zircon thermochronology has a remarkable agreement with the mineralogical and K–Ar data (Table 5). In areas where the clay mineralogy-based maximum palaeotemperatures exceed 180 °C the ZHe ages are totally reset and range from 82 to 34 Ma (structural domains SD1, SD2, SD4 and SD5). In Middle Triassic rocks of SD8 where the illite–smectite maximum palaeotemperature (118–156 °C; Table 5) is below the ZHe reset range the ZHe age is much older (213 Ma) and represent detrital age with only minor rejuvenation. Thus the reset of the ZHe chronometer is in agreement with estimates of the

Table 4
Peak broadening (FWHM – full width at half maximum) of the 104 reflection of haematite in the rocks under study, compared with samples from other basins of known maximum palaeotemperatures.

Velebit	104 FWHM	Tatra[a]	104 FWHM	Podolia[b]	104 FWHM	Upper Silesia[c]	104 FWHM	Kowala[d]	104 FWHM
Triassic	°2q	Triassic	°2q	Devonian	°2q	Triassic	°2q	Permian	°2q
Vel-4	0.21	IWA-0	0.36	Zalish-3	0.29	K-1/26.7	0.55	Kow-47	0.66
Vel-10	0.21	IWA-1	0.31	Zalish-5	0.33	K-1/28.5	0.51	Kow-48	0.6
Vel-16	0.23	IWA-2	0.33			K-1/29.8	0.5	Kow-49	0.54
Vel-18	0.23	IWA-3	0.22			KOB-45.4	0.48		
Vel-19	0.23	IWA-4	0.24			KOB-53.4	0.48		
Vel-21	0.19	TOM-4	0.25			PAT-38	0.49		
Vel-23	0.32	TOM-6	0.32			PAT-44	0.49		
Vel-36	0.3	TOM-7	0.26			PAT-62.6	0.46		
Vel-46	0.23	Cz.Ż-3	0.35						
Vel-69	0.24	Cz.Ż-12	0.26						
Vel-97	0.22	Cz.Ż-14	0.23						
		Cz.Ż-15	0.3						
Mean	0.24		0.29		0.31		0.5		0.6
Palaeotemp.			200–270 °C		ca. 200 °C		ca. 125 °C		ca. 120 °C

[a] Środoń et al., 2006b.
[b] Środoń et al., 2013.
[c] Środoń et al., 2014.
[d] Środoń, unpublished data.

maximum palaeotemperatures based on the illite–smectite composition. In structural domains SD1, SD2, SD4 and SD5 the fully reset ZHe ages are close to the corresponding K–Ar ages, representing the maximum palaeotemperature period.

All AFT ages are at least 120 Ma younger than the stratigraphic ages (80 to 24 Ma), their overall reset is consistent with the illite–smectite-based palaeotemperatures exceeding ~120 °C in all areas where AFT ages were measured.

6. Modelling thermal histories of the structural domains

The thermal history was modelled by the HeFTy software of Ketcham (2005). The considered input data were the AHe and ZHe ages, crystal sphere radius, U and Th concentrations, fission track counts, AFT age, confined track length distribution and the measured kinetic parameter (Dpar). The following constraints were considered: (i) the age of deposition, (ii) the maximum burial temperature as detected by clay mineralogy, and (iii) the annual mean surface temperature. Otherwise the modelling runs were performed in unconstrained mode. The modelling of the thermal history was performed on selected samples that represent the clusters of samples collected in a given structural domain. Except for the two oldest ZHe ages, the apatite and zircon thermochronological data are considerably younger than the age of deposition. Therefore we did not consider the pre-depositional thermal history of the detrital grains of arenites.

The modelling results are compiled in Fig. 9. For the majority of samples the modelling is based on both the AFT and ZHe data, and thus these thermal histories are well constrained. For two samples the modelled paths are based only on one method (Va-4a: AFT, Vel-28: ZHe), so these two thermal histories are poorly constrained. In both cases another sample with well constrained thermal history has been studied from the same structural domain (Fig. 9).

SD1 yielded variable AFT ages (Table 3). The extreme differences in apparent ages of samples from the same outcrop (Va-4 and Va-4a) can be explained by different chemistry of the samples (Table 3). Sample Va-4a has bigger Dpar, which is due probably to a higher Cl content. The difference between sample Va-2 (55 Ma) and samples Va-1 and Vel-7 (28 Ma) (Fig. 2) can be explained by a closer position of the latter two to the Brušane–Oštarije Fault. The thermal history was modelled for two localities: while Va-4a is based only on AFT data, the analysis for the combined samples Va-1 and Vel-7 considers both methods, implying narrower confidence belt (Fig. 9). The maximum temperature of sample Va-4a could have been higher because AFT provides constraints for the minimum temperature only. The beginning of cooling of SD1 is around 90–80 Ma, consistent for both localities. The modelling of the combined sample using both methods yielded a break in post-Cretaceous cooling with an accelerated cooling period during and after the Late Eocene to Oligocene.

For SD2 the clay mineralogical data indicate that the Carboniferous and the Permian formations experienced maximum temperature above 200 °C. The ZHe apparent ages are partly similar to the Late Cretaceous age detected in SD1, but in sample Vel-28 the ZHe apparent age is much younger. The difference in the apparent ages can be explained by the different vertical position of the samples in the stratigraphic column, however, it must be noted that the samples of SD2 were collected relatively close to the border faults of this domain. The beginning of cooling here is around 70–60 Ma.

In SD3, SD4 and SD5 the apparent ages and the modelled thermal paths are rather similar. This is remarkable, as these domains are separated by significant thrust faults of km-scale offsets. The common features of these domains include Cretaceous thermal climax, and highest cooling rate during the latest Cretaceous to Palaeogene, after a sharp beginning of cooling which occurs at 80–70 Ma in SD4 and SD 5 and somewhat earlier at 110–100 Ma in SD3. The obtained data suggest that these domains experienced a rapid denudation by weathering and erosion contemporaneous with a rock uplift during the Late Eocene to Early Oligocene thrusting. In other words, we can presume that during that period the rate of denudation have either balanced or at times even surpassed the amount of tectonic uplift in this part of the study area, because a substantial part or the entire thickness of the overthrusting strata has been rapidly removed and thus did not thermally affected the underlying Palaeozoic and Triassic strata of SD4 and SD5 domains.

SD6 experienced lower maximum temperature than the domains situated to the SW of the Split–Karlovac Fault, as suggested by the thermal modelling and the apparent ZHe age of the Lower Triassic sandstone, which is Triassic and indicates only minor partial reset. A less pronounced beginning of cooling is recognized around 70–60 Ma. The modelling shows a complex thermal history for the Neogene. Its explanation is not trivial, as neither Neogene igneous activity nor significant basin subsidence and exhumation is known from the region of SD6. However, it might be explained by its position close to the Split–Karlovac Fault, which has a complex kinematic history (see Section 2.3). This structural element has recently been considered as the major dextral transfer fault linking the Miocene thrust front in the Southern Alps with contemporaneously active orogenic front in the southern Karst Dinarides (Handy et al., 2014).

Table 5

Synopsis of geothermometric and geochronological results (Tables 1–3) obtained for the eight structural units of the central part of the Karst Dinarides, listed along with the age of onset cooling from Fig. 9 and the estimates of sedimentary burial depth at the end of Cretaceous from Fig. 3. Thermal palaeogradients at the end of the Cretaceous calculated from the maximum palaeotemperatures from %S minus assumed surface palaeotemperature and the values of sedimentary burial depth. Average exhumation rates calculated from the age of onset cooling and the sedimentary burial depth plus present elevation a.s.l. The latter is compared to the elevation a.s.l. calculated assuming the surface uplift rate as 10–15% of the exhumation rate.

Struct. Domain	Sample	Stratigr. Age	Max. PaleoT from %S	Max. PaleoT from K-Ar	Max. PaleoT from K, P, Py	Max. PaleoT modelled	K-Ar age	ZHe age	AFT age	AHe age	Modelled start cooling	Sed. Burial depth MIN	Sed. Burial depth MAX	Calc. paleogr.	Calc. paleogr.	Exhumation rate	Exhumation rate	Calc. elev. a.s.l.	Elev. a.s.l.
			[°C]	[°C]	[°C]	[°C]	[Ma]	[Ma]	[Ma]	[Ma]	[Ma]	[km]	[km]	[°C/km]	[°C/km]	m/Ma	m/Ma	m	m
SD1	Va-4	T2_3							40.6 ± 8.5										
SD1	Va-4a	T2_3							79.9 ± 9.1										
SD1	Va-2	T2							55.4 ± 12.1										
SD1	PL-9	T2	126				< 49		nd			3.8	4.4	28	24				
SD1	Va-1								28.1 ± 5.3										
SD1	Vel-10	T2	250		< 270		< 84		nd			3.8	4.4	61	52				
SD1	Vel-7	T2				140		90.9-76.5	27.9 ± 6.3		80	3.8	4.4			57	64	484-727	736
SD2	Vel-74	T2_3						73.8-72.0	nd										
SD2	Vel-72G	T2_3	184				< 73		nd			3.6	3.8	46	43				
SD2	Va-24	T2_3							33.1 ± 6.2										
SD2	Vel-96	T2							55.9 ± 5.9										
SD2	Vel-95	T2							54.6 ± 5.8										
SD2	Va-12	P1,2							67.8 ± 15.4										
SD2	Va-13	P1,2							37.3 ± 5.1										
SD2	Va-10	P1,2							42.1 ± 5.9										
SD2	Va-11	P1,2							37.6 ± 4.6										
SD2	Vel-18	P1,2	211		> 200				nd			5.6	5.8	34	33				
SD2	Va-14	P1,2							38.1 ± 5.0										
SD2	Vel-20	P1,2							53.2 ± 6.6										
SD2	Vel-98	P1,2				180		79.9-40.9	27.4 ± 6.1		70	5.6	5.8			89	92	633-950	663
SD2	Va-7	T1							43.1 ± 4.3	52.9-37.2									
SD2	Va-8	T1							40.9 ± 3.6										
SD2	Va-5	C2							55.8 ± 7.5										
SD2	Vel-26	C	250	200-300	> 200				nd			6	6.2	38	37				
SD2	Vel-28	C-P				190		49.6-41.1	nd		60	6	6.2			110	113	669-1004	585
SD2	Va-25	T2_3							28.7 ± 3.2										
SD2	Va-26	T2_3							35.7 ± 5.2										
SD3	NPP-421	P				170		139.6-72.4	nd		100	4.6	4.7			55	56	555-832	858
SD3	NPP-420	T1							66.3 ± 6.5										
SD4	Vel-57	T2					< 61		nd										
SD-4	Vel-62	T2	206						nd			3.9	4.2	48	44				
SD4	Va-17	T2							45.5 ± 6.5										
SD4	Va-16	T2				180			36.8 ± 5.1		70	3.9	4.2			64	68	462-693	577
SD4	Vel-30	C2	250	200-300	close to 270				nd			6	6.3	38	37				
SD4	Va-18	C2				180		80.5-43.4	nd		70	6	6.3			94	99	675-1913	612
SD4	Vel-34	C2						94.0-55.7	34.9 ± 6.5										

(continued on next page)

Table 5 (*continued*)

Struct. Domain	Sample	Stratigr. Age	Max. PaleoT from % S	Max. PaleoT from K-Ar	Max. PaleoT from K, P, Py	Max. PaleoT modelled	K-Ar age	ZHe age	AFT age	AHe age	Modelled start cooling	Sed. Burial depth MIN	Sed. Burial depth MAX	Calc. paleogr.	Calc. paleogr.	Exhumation rate	Exhumation rate	Calc. elev. a.s.l.	Elev. a.s.l.
			[°C]	[°C]	[°C]	[°C]	[Ma]	[Ma]	[Ma]	[Ma]	[Ma]	[km]	[km]	[°C/km]	[°C/km]	m/Ma	m/Ma	m	m
SD4	Vel-33	C							30.5 ± 7.9										
SD4	Ve-47	C	130		close to 270							6	6.3	18	17				
SD5	Vel-45	T3					< 77		nd										
SD5	Va-31	T3							23.6 ± 3.0	37.7-28.2									
SD5	Vel-38	T2	250		> 200				nd			3.9	4	59	58				
SD5	Vel-39	T2				180		97.2-44.9	nd		70	3.9	4			66	68	469-703	745
SD5	Va-20	T2				180			34.1 ± 4.0		70	3.9	4			66	68	469-703	745
SD5	Vel-44	T2							31.5 ± 5.4										
SD6	P-2	T1				120		235.1-190.8	48.7 ± 4.0		60	5.5	6			97	105	606-909	321
SD6	P-3	T1							53.8 ± 4.9										
SD6	P-1	T1							50.3 ± 5.4										
SD7	PL-4/1	J3	70				< 60		nd			2.2	2.4	23	21				
SD8	S-4	T2				120		256.8-157.3	69.0 ± 9.3		90	4.8	4.9			62	63	562-844	808
SD8	PL-13/1	T2	118						nd			4.8	4.9	20	20				
SD8	PL-13/5	T2	156						nd			4.8	4.9	28	28				
SD8	S-1	T1				150		116.1-90.5	34.6 ± 3.5	35.1-28.3	70	5.6	5.6			89	89	623-934	656

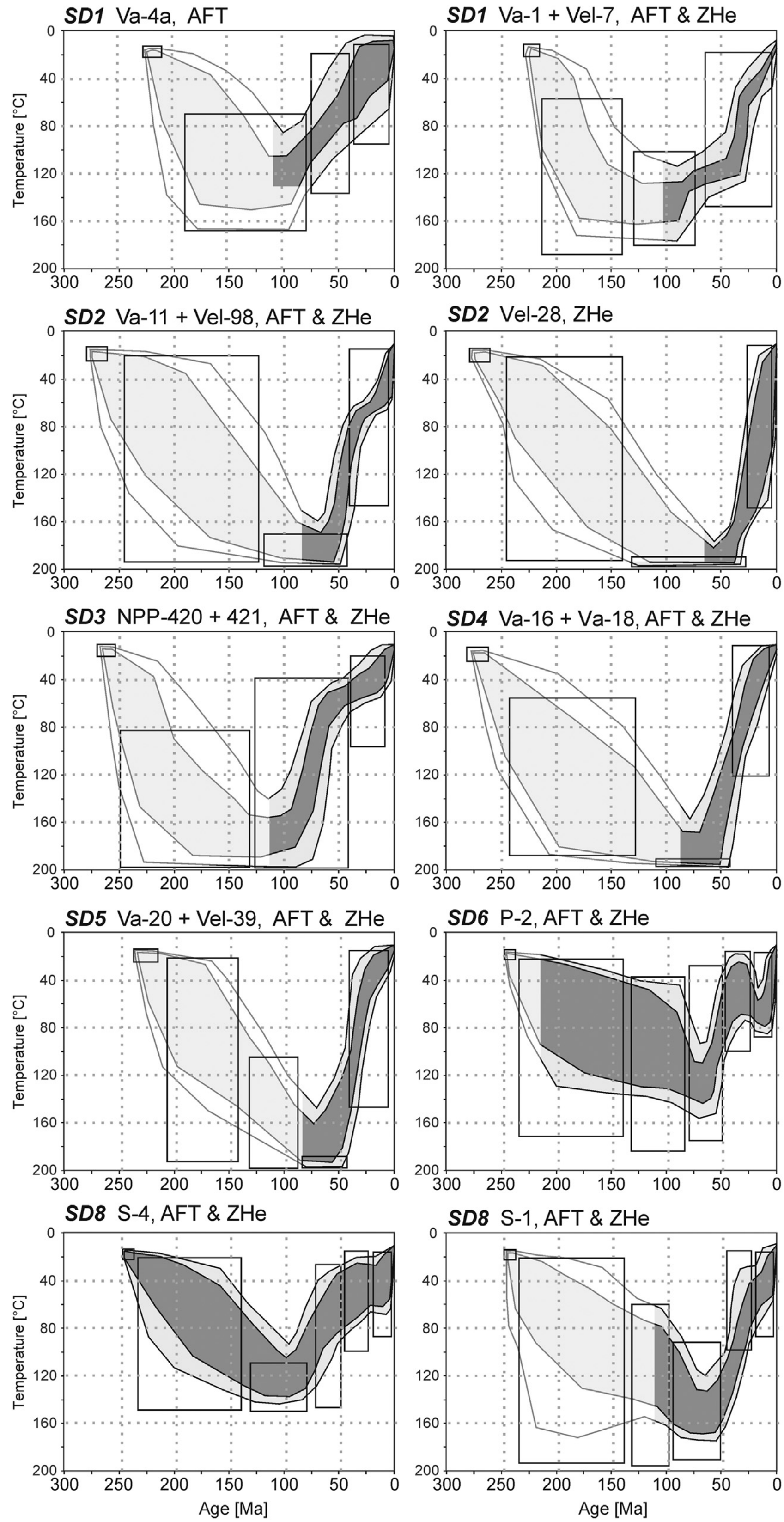

Fig. 9. Results of thermal modelling performed by HeFTy software (Ketcham, 2005). The structural domain, the sample numbers and the types of applied thermochronological data are indicated. The boxes represent the time–temperature constraints applied to modelling runs. The pale fields indicate the time–temperature ranges where the modelling results should not be considered as the thermochronological memory of the earlier part of the evolution was erased by younger high temperature event. See the text for details of the modelling settings.

In SD7 it was possible to collect only one sample for clay mineral analysis. This single data confirm that southeastern domains (SD6–SD8) experienced weaker thermal overprint than the northwestern domains (SD1–SD5). However, the studied sample comes from the Jurassic sequence and thus represents a shallower stratigraphic level than the majority of samples collected from the upper Palaeozoic and Triassic formations.

The two Triassic samples from SD8 yield different ZHe apparent ages. The difference between these ages cannot be explained by the variation in radiation damage densities as the effective uranium contents in the dated zircons are similar. We assume that the stratigraphic position of the samples is the reason for the difference in the ZHe ages: the deep-seated Lower Triassic sample S-1 experienced higher burial temperature and yields Cretaceous ZHe age (103 Ma), while the Middle Triassic sample S-4 yields a partial reset age of 213 Ma. The thermal modelling, which is based on ZHe and AFT data for both samples, shows thermal evolutions that are basically similar to other domains with the beginning of cooling between 90 and 70 Ma, but the maximum palaeotemperatures of the samples are again lower (ca. 120 °C and ca. 150 °C) when compared to the northwestern domains (SD1–SD5). The vertical distance between the two samples is ca. 850 m, which suggests a geothermal gradient of approx. 35 °C/km at the time of maximum palaeotemperature.

As a summary we can conclude that all studied domains were affected by an abrupt change in burial temperature when cooling started between 100 and 60 Ma (Late Cretaceous to Palaeocene). This result is consistent with the ages of maximum palaeotemperature as estimated from the K–Ar data. Some samples indicate constant cooling rates, other samples indicate variable cooling rates, with a distinct Cenozoic cooling period.

7. Thermo-tectonic evolution

Our analyses allow estimating the maximum palaeotemperatures in different structural domains in the central part of the Karst Dinarides, the age of the thermal climax, and the character of the post-climax cooling paths. The event best constrained by our data is rapid cooling, which started in different tectonic domains between 80 and 35 Ma, i.e. in the period when the major phase of a carbonate sedimentation ended and the platform mostly emerged and became disintegrated. Such timing implies that our thermochronological data indicate maximum palaeotemperatures corresponding to sedimentary burial at the end of the Cretaceous. This is a surprising result, because it would be more intuitive to expect the peak of palaeotemperature during subsequent tectonic burial related to SW-directed thrusting, which took place in the Late Eocene to Oligocene, at least in those structural domains occupying lower structural positions with respect to neighbouring domains (e.g. SD5 and SD4).

Such result was tested by calculating palaeogeothermal gradients (Table 5) from the illite–smectite palaeotemperatures and the estimated maximum sedimentary overburden data (Fig. 3). The surface mean temperature was estimated at 20 °C, i.e. 5 °C higher than present, because of a much more southern location of the area at the end of Cretaceous which was also a period characterized by generally warm climate (position was around 30–35°N at 80–60 Ma; Scotese, 2002). The calculated palaeogeothermal gradients should be considered only as rough estimates, in particular when using the palaeotemperatures above 200 °C, which are rather inaccurate and could have been substantially lower. The lowest estimate (Vel-47, SD4) is also doubtful, because this sample contains paragonite, implying that the palaeotemperature most probably was substantially higher. The remaining values fall into 48–20 °C/km range (30–32 °C/km average), with the tendency to decrease in the SE part of the study area (21–28 °C/km; Table 5).

The current value of geothermal gradient in the Karst Dinarides is lower, around 10–20 °C/km (Jelić et al., 1995). The elevated, mountainous topography, the intense winter precipitation and the highly permeable karst make the study area a well-developed recharge zone and that is why the top level of the crust is strongly chilled here. Substantially higher values are expected for the time before the build-up of the current topography. Also, the Late Cretaceous around 80 Ma ago was characterized by magmatic intrusions recorded northwards in the area of neighbouring Inner Dinarides (Ustaszewski et al., 2009). In conclusion, the calculated palaeogeothermal gradient values make the end-of-Cretaceous sedimentary burial hypothesis feasible.

This conclusion bears also consequences for the tectonic history of the Velebit Mt. It implies that the potential tectonic burial, related either to the thin-skinned top-SW thrusting (Tari-Kovačić and Mrinjek, 1994; Tari, 2002) or to the top-NE thrusting of a passive roof duplex system (Tomljenović et al., 2017), in structurally underlying units never surpassed the sedimentary burial temperatures. Therefore, the tectonic burial in the studied part of the Velebit Mt. must have been accompanied by a rapid denudation by weathering and erosion. However, in other structural domains (e.g. SD1, SD6, SD8; Fig. 9) the strong variations and reversals on the cooling curves, visible for some samples in the Cenozoic might correspond to the tectonic-related burial.

The estimated maximum sedimentary overburden data (Fig. 3) and present elevation a.s.l. (Table S1) combined with the age of the onset of cooling (Fig. 9) allow the estimation of the vertical exhumation rates (Table 5), under the feasible assumption that cooling is related to the uplift and erosion. The calculation turns out 55–65 m/Ma rates for the domains with > 70 Ma onset of cooling and 65–110 m/Ma for the domains with < 70 Ma onset of cooling. These numbers are at least an order of magnitude lower than the exhumation rates in high mountains (e.g. Burbank, 2002), which seems consistent with the relatively low elevation of the area. The surface uplift rate accounts typically for 10–15% of the exhumation rate. If these values and the age of onset of cooling are used, the calculated elevations a.s.l. come close to the actual values (Table 8), which additionally supports presented model indicating a long-term balance of the tectonic uplift and the denudation rates.

8. Conclusions

Clay mineralogy, combined with illite–smectite K–Ar dating, fission track and (U–Th–Sm)/He thermochronology of apatite and zircon crystals provided a consistent data set for the reconstruction of thermal history of the carbonate-dominated succession in the central part of the Karst Dinarides.

The maximum palaeotemperatures were determined as > 200 °C but not exceeding 270 °C, and were lower in the southeastern study area (ca. 150 °C). The illite K–Ar ages of the Triassic samples together with the results of thermal modelling indicate that in most of the structural domains the thermal climax was reached during the Late Cretaceous and thus it is related to sedimentary burial at palaeogeothermal gradients significantly higher than the present. The cooling started between 80 and 35 Ma, usually it was first rapid and slowed down later. A distinct Eocene/Oligocene cooling phase has also been detected. The calculated average exhumation rates are very variable and range from 55 to 110 m/Ma. The thickness of sediment column removed by erosion from above the present-day topography varies between 6 and 6.3 km for the Carboniferous strata and 2.2–2.4 km for the Jurassic rocks. These are minimum estimates, not accounting for the tectonic burial.

A methodological message emerged from the study of red continental sediments: at burial temperatures above 120 °C sedimentary haematite undergoes structural reorganization, resulting in significant change of its XRD characteristics. This finding explains the reset of the haematite magnetic properties well below its Curie temperature (675 °C), as observed and dated as Cretaceous by Werner et al. (2015), which is consistent with our estimation of the age of the maximum palaeotemperatures.

Acknowledgements

We thank Marta Mileusnić for her help during the field work. Leszek Chudzikiewicz helped with drawing some figures. This study was mostly funded by the project no. N N307 475238 granted to Marek Lewandowski by the Polish Ministry of Science and Higher Education, and in part by Croatian Science Foundation under the project IP-2014-09-9666 "Velebit Top to Bottom – Multi-Disciplinary Research Linking Seismological Data and Tectonics in the Mt. Velebit Region" (PI Marijan Herak). Projects "K–Ar" and "ATLAB" of the Institute of Geological Sciences, P.A.S. are also acknowledged. We are grateful to INA Industrija Nafte d.d. oil company which gave us permission to present the data from Dabar and Svilaja in this publication. We would also like to thank the reviewers Jocelyn Barbarand and Franz Neubauer for their valuable comments which significantly improved the quality of the paper.

Appendix A. Supplementary data

Supplementary data to this article can be found online at https://doi.org/10.1016/j.tecto.2018.06.016. These data include the Google map of the most important areas described in this article.

References

Aljinović, D., Isozaki, Y., Sremac, J., 2008. The occurrence of giant bivalve Alatoconchidae from the Yabeina zone (Upper Guadalupian, Permian) in European Tethys. Gondwana Res. 13, 275–287.
Altaner, S.P., Hower, J., Whitney, G., Aronson, J.L., 1984. Model for K-bentonite formation: evidence from zoned K-bentonites in the disturbed belt, Montana. Geology 12, 412–415.
Anceau, A., 1992. Sudoite in some Visean (Lower Carboniferous) K-bentonites from Belgium. Clay Miner. 27, 283–292.
Babić, L., Hernitz-Kučenjak, M., Ćorić, S., Zupanič, J., 2007. The Middle Eocene age of the supposed Late Oligocene sediments in the flysch of the Pazin Basin (Istria, Outer Dinarides). Natura Croatica 16, 83–103.
Babić, L., Crnjaković, M., Asmerom, Y., 2012. Uplifted Pleistocene marine sediments of the Central Adriatic Island of Brusnik. Geologia Croatica 65 (2), 223–232.
Bahun, S., 1963. Geološki odnosi okolice Donjeg Pazarišta u Lici (trijas i tecijarne Jelarnaslage). Geol. Vjesn. 16, 161–170.
Bahun, S., 1974. The tectogenesis of Mt. Velebit and the formation of Jelar-deposits. Geol. Vjesn. 27, 35–51.
Barbarand, J., Carter, A., Wood, I., Hurford, T., 2003. Compositional and structural control of fission-track annealing in apatite. Chem. Geol. 198, 107–137.
Benac, C., Juračić, M., Blašković, I., 2008. Tidal notches in Vinodol Channel and Bakar Bay, NE Adriatic Sea: indicators of recent tectonics. Mar. Geol. 248, 151–160.
Benetatos, C., Kiratzi, A., 2006. Finite-fault slip models for the 15 April 1979 (Mw 7.1) Montenegro earthquake and its strongest aftershock of 24 May 1979 (Mw 6.2). Tectonophysics 421, 129–143.
Bennett, R.A., Hreinsdóttir, S., Buble, G., Bašić, T., Bačić, Ž., Marjanović, M., Casale, G., Gendaszek, A., Cowan, D., 2008. Eocene to present subduction of southern Adria mantle lithosphere beneath the Dinarides. Geology 36, 3–6.
Bergmann, J., Kleeberg, R., 1998. Rietveld analysis of disordered layer silicates. In: Delhez, R., Mittemeijer, E.J. (Eds.), EPDIC 5 – Proc. European Powder Diffraction Conf. Mat. Sci. Forum. 278–281. pp. 300–305.
Biernacka, J., 2014. Pore-lining sudoite in Rotliegend sandstones from the eastern part of the southern Permian Basin. Clay Miner. 49, 635–655.
Blašković, I., 1988. The two stages of structural formation of the coastal belt of the External Dinarides. Geologia Croatica 51 (1), 75–89.
Brindley, G.W., Brown, G., 1980. Crystal structures of clay minerals and their X-ray identification. In: Mineralogical Society Monograph. 5 (495 pp., London).
Burbank, D.W., 2002. Rates of erosion and their implications for exhumation. Mineral. Mag. 66, 25–52.
Burtner, R.L., Nigrini, A., Donelick, R.A., 1994. Thermochronology of Lower Cretaceous source rocks in the Idaho–Wyoming thrust belt. AAPG Bull. 78, 1613–1636.
de Capoa, P., Radoičić, R., D'Argenio, B., 1995. Late Miocene deformation of the External Dinarides (Montenegro and Dalmatia). New biostratigraphic evidence. Sci. Geol. Mem. 47, 157–172.
Caporali, A., Aichhorn, C., Barlik, M., Becker, M., Fejes, I., Gerhatova, L., Ghitau, D., Grenerczy, G., Hefty, J., Krauss, S., Medak, D., Milev, G., Mojzes, M., Mulic, M., Nardo, A., Pesec, P., Rus, T., Simek, J., Sledzinski, J., Solaric, M., Stangl, G., Stopar, B., Vespe, F., Virag, G., 2009. Surface kinematics in the Alpine–Carpathian–Dinaric and Balkan region inferred from a new multi-network GPS combination solution. Tectonophysics 474, 295–321.
Carlson, W.D., Donelick, R.A., Ketcham, R.A., 1999. Variability of apatite fission-track annealing kinetics: I. Experimental results. Am. Mineral. 84, 1213–1223.
Chorowicz, J., 1975. Mechanics of Split–Karlovac transversal structure in Yugoslavian Dinarides. C. R. Acad. Sci. D 280 (20), 2313–2316.
Chorowicz, J., 1977. Etude géologique des Dinarides le long de la structure transversale Split–Karlovac (Yougoslavie). Ann. Soc. Géol. Nord 1 (331 pp.).
Clauer, N., Środoń, J., Franců, J., Šucha, V., 1997. K–Ar dating of illite fundamental particles separated from illite–smectite. Clay Miner. 32, 181–196.
Dedić, Ž., Ilijanić, N., Miko, S., 2018. A mineralogical and petrographic study of evaporites from the Mali Kukor, Vranjkovići, and Slane Stine deposits (Upper Permian, Dalmatia, Croatia). Geologia Croatica 71 (1), 19–28.
Djimbi, M.D., Gautheron, C., Roques, J., Tassan-Got, L., Gerin, C., Simoni, E., 2015. Impact of apatite chemical composition on (U–Th)/He thermochronometry: an atomistic point of view. Geochim. Cosmochim. Acta 167, 162–176.
Donelick, R.A., Ketcham, R.A., Carlson, W.D., 1999. Variability of apatite fission-track annealing kinetics: II. Crystallographic orientation effects. Am. Mineral. 84, 1224–1234.
Donelick, R.A., O'Sullivan, P.B., Ketcham, R.A., 2005. Apatite fission-track analysis. Rev. Mineral. Geochem. 58, 49–94.
Dumitru, T.A., 1993. A new computer automated microscope stage system for fission-track analysis. Nucl. Tracks Radiat. Meas. 21, 575–580.
Dunkl, I., 2002. TRACKKEY: a windows program for calculation and graphical presentation of fission track data. Comput. Geosci. 28 (2), 3–12.
Faivre, S., Fouache, E., Kovačić, V., Glušćević, S., 2010. Some geomorphological and archaeological indicators of Croatian shoreline evolution over the last 2000 years. In: Geology of the Adriatic Area. GeoActa Special Publication 3. pp. 125–133.
Farley, K.A., Wolf, R.A., Silver, L.T., 1996. The effects of long alpha-stopping distances on (U–Th)/He ages. Geochim. Cosmochim. Acta 60, 4223–4229.
Ferreiro Mählmann, R.F., 2001. Correlation of very low grade data to calibrate a thermal maturity model in a nappe tectonic setting, a case study from the Alps. Tectonophysics 334, 1–33.
FGI, 1970. Geological Map of SFR Yugoslavia 1:500,000. Federal Geological Institute, Beograd.
Fio, K., Spangenberg, J.E., Vlahović, I., Sremac, J., Velić, I., Mrinjek, E., 2010. Stable isotope and trace element stratigraphy across the Permian–Triassic transition: a redefinition of the boundary in the Velebit Mountain, Croatia. Chem. Geol. 278, 38–57.
Fleet, M.E., 2003. Micas. Volume 3A of Rock Forming Minerals. The Geological Society, London (765 pp.).
Flowers, R.M., Ketcham, R.A., Shuster, D.L., Farley, K.A., 2009. Apatite (U–Th)/He thermochronometry using a radiation damage accumulation and annealing model. Geochim. Cosmochim. Acta 73, 2347–2365.
Frey, M., 1987. Low Temperature Metamorphism. Blackie, Glasgow and London (351 pp.).
Galbraith, R.F., 1981. On statistical models for fission track counts. Math. Geol. 13, 471–478.
Galbraith, R.F., Laslett, G.M., 1993. Statistical models for mixed fission track ages. Nucl. Tracks Radiat. Meas. 21, 459–470.
Gautheron, C., Tassan-Got, L., Barbarand, J., Pagel, M., 2009. Effect of alpha-damage annealing on apatite (U–Th)/He thermochronology. Chem. Geol. 266, 157–170.
Gautheron, C., Espurt, N., Barbarand, J., Roddaz, M., Baby, P., Brusset, S., Tassan-Got, L., Douville, E., 2013. Direct dating of thick- and thin-skin thrusts in the Peruvian Subandean zone through apatite (U–Th)/He and fission track thermochronometry. Basin Res. 25, 1–17.
Gleadow, A.J.W., 1981. Fission track dating methods: what are the real alternatives? Nucl. Tracks 5, 3–14.
Gleadow, A.J.W., Duddy, I.R., 1981. A natural long term annealing experiment for apatite. Nucl. Tracks 5, 169–174.
Gleadow, A.J.W., Duddy, I.R., Lovering, J.F., 1983. Fission track analysis: a new tool for the evaluation of thermal histories and hydrocarbon potential. J. Aust. Petrol. Explor. Assoc. 23, 93–102.
Gleadow, A.J.W., Duddy, I.R., Green, P.F., Hegarty, K.A., 1986. Fission track lengths in the apatite annealing zone and the interpretation of mixed ages. Earth Planet. Sci. Lett. 78, 245–254.
Gleadow, A.J.W., Belton, D.X., Kohn, B.P., Brown, R.W., 2002. Fission track dating of phosphate minerals and thermochronology of apatite. Rev. Mineral. Geochem. 48 (1), 579–630. http://dx.doi.org/10.2138/rmg.2002.48.16.
Green, P.F., 1981. 'Track-in track' length measurements in annealed apatites. Nucl. Tracks 5, 12–18.
Green, P.F., 1986. On the thermo-tectonic evolution of northern England: evidence from fission track analysis. Geol. Mag. 153, 493–506.
Green, P.F., Duddy, I.R., 1989. Some comments on paleotemperature estimation from apatite fission track analysis. J. Pet. Geol. 12, 111–114.
Green, P.F., Duddy, I.R., Gleadow, A.J.W., Tingate, P.R., Laslett, G.M., 1986. Thermal annealing of fission tracks in apatite 1. A qualitative description. Chem. Geol. 59, 237–253.
Grenerczy, G., Sella, G., Stein, S., Kenyeres, A., 2005. Tectonic implications of the GPS velocity field in the northern Adriatic region. Geophys. Res. Lett. 32, L16311. http://dx.doi.org/10.1029/2005GL022947.
Grimani, I., Šikić, K., Šimunić, A., 1972. Osnovna geološka karta SFRJ 1:100000. List Knin L33–141 (Basic Geological Map of SFRJ 1:100000. Knin Sheet). Institut za geološka istraživanja Zagreb, Savezni geološki zavod, Beograd.
Guenthner, W.R., Reiners, P.W., Ketcham, R.A., Nasdala, L., Giester, G., 2013. Helium diffusion in natural zircon: radiation damage, anisotropy, and the interpretation of zircon (U–Th)/He thermochronology. Am. J. Sci. 313 (3), 145–198.
Handy, M., Ustaszewski, K., Kissling, E., 2014. Reconstructing the Alps–Carpathians–Dinarides as a key to understanding switches in subduction polarity, slab gaps and surface motion. Int. J. Earth Sci. 104, 1–26. http://dx.doi.org/10.1007/s00531-014-1060-3.
Herak, M., 1991. Dinaridi – mobilistički osvrt na genezu i strukturu (Dinarides – mobilistic view of the genesis and structure). Acta Geol. 21 (2), 35–117.

Herak, D., Herak, M., Prelogović, E., Markušić, S., Markulin, Ž., 2005. Jabuka island (Central Adriatic Sea) earthquakes of 2003. Tectonophysics 398, 167–180.
Heuser, M., Andrieux, P., Petit, S., Stanjek, H., 2013. Iron-bearing smectites: a revised relationship between structural Fe, b cell edge lengths and refractive indices. Clay Miner. 48, 97–103.
Hillier, S., 2003. Chlorite in sediments. In: Middleton, G.V. (Ed.), Encyclopedia of Sediments and Sedimentary Rocks. Kluwer Academic Publishers, Dordrecht–Boston–London, pp. 123–127.
Hillier, S., Wilson, M.J., Merriman, R.J., 2006. Clay mineralogy of the Old Red Sandstone and Devonian sedimentary rocks of Wales, Scotland and England. Clay Miner. 41, 433–471.
Hourigan, J.K., Reiners, P.W., Brandon, M.T., 2005. U–Th zonation-dependent alpha-ejection in (U–Th)/He chronometry. Geochim. Cosmochim. Acta 69, 3349–3365.
Hunziker, J.C., Frey, M., Clauer, N., Dallmeyer, R.D., Friedrichsen, H., Flehmig, W., Hochstrasser, K., Roggwiler, P., Schwander, H., 1986. The evolution of illite to muscovite: mineralogical and isotopic data from the Glarus Alps, Switzerland. Contrib. Mineral. Petrol. 92, 157–180.
Hurford, A.J., 1990a. International Union of Geological Sciences Subcommission on Geochronology recommendation for the standardization of fission track dating calibration and data reporting. Nucl. Tracks 17, 233–236.
Hurford, A.J., 1990b. Standardization of fission track dating calibration: recommendation by the Fission Track Working Group of the I.U.G.S. Subcommission on Geochronology. Chem. Geol. 80, 171–178.
Hurford, A.J., 1998. ZETA: the ultimate solution to fission-track analysis calibration or just an interim measure. In: Van den Haute, P., De Corte, F. (Eds.), Advances in Fission-track Geochronology. Kluwer Academic Publishers, pp. 19–32.
Hurford, A.J., Green, P.F., 1983. The age calibration of fission-track dating. Isot. Geosci. 1, 285–317.
Ivanović, A., Sakač, K., Marković, B., Sokač, B., Šušnjar, M., Nikler, L., Šušnjara, A., 1973. Osnovna geološka karta SFRJ 1:100000. List Obrovac L33–140 (Basic Geological Map of SFRJ 1:100000. Obrovac Sheet). Institut za geološka istraživanja Zagreb, Savezni geološki zavod, Beograd.
Ivanović, A., Sakač, K., Sokač, B., Vrsalović-Carević, J., Zupanič, J., 1976. Osnovna geološka karta SFRJ 1:100000. Tumač za list Obrovac L33–140 (Basic Geological Map of SFRJ 1:100000. Geology of the Obrovac Sheet). Institut za geološka istraživanja Zagreb, Savezni geološki zavod, Beograd, pp. 1–61.
Ivanović, A., Sikirica, V., Marković, S., Sakač, K, 1977. Osnovna geološka karta SFRJ 1:100000. List Drniš K33–9 (Basic Geological Map of SFRJ 1:100000. Drniš Sheet). Institut za geološka istraživanja Zagreb, Savezni geološki zavod, Beograd.
Jackson, M.L., 1975. Soil Chemical Analysis – Advanced Course. Published by the author, Madison, Wisconsin.
Japundžić, M., Sremac, J., 2016. Palaeobiogeography of the Late Carboniferous brachiopoda from Velebit Mt. (Croatia). Geologia Croatica 69 (2), 177–185.
Jelić, K., Kevrić, I., Krasić, O., 1995. Temperature i toplinski tok u tlu Hrvatske (Temperatures and heat flux in the Croatian territory – in Croatian). In: Vlahović, I., Velić, I., Šparica, M. (Eds.), 1st Croatian Geological Congress, Opatija, October 18–21, 1995., Proceedings 1, Zagreb, pp. 245–249.
Kastelic, V., Carafa, M.M.C., 2012. Fault slip rates for the active External Dinarides thrust and–fold belt. Tectonics 31, TC3019. http://dx.doi.org/10.1029/2011TC003022.
Kastelic, V., Vannoli, P., Buratto, P., Fracassi, U., Tiberti, M.M., Valensise, G., 2013. Seismogenic sources in the Adriatic domain. Mar. Pet. Geol. 42, 191–213.
Ketcham, R., 2005. Forward and inverse modeling of low-temperature thermochronometry data. Rev. Mineral. Geochem. 58, 275–314.
Ketcham, R.A., Carter, A., Donelick, R.A., Barbarand, J., Hurford, A.J., 2007a. Improved measurement of fission track annealing in apatite using c-axis projection. Am. Mineral. 92, 789–798.
Ketcham, R.A., Carter, A., Donelick, R.A., Barbarand, J., Hurford, A.J., 2007b. Improved modeling of fission track annealing in apatite. Am. Mineral. 92, 799–810.
Korbar, T., 2009. Orogenic evolution of the External Dinarides in the NE Adriatic region: a model constrained by tectonostratigraphy of Upper Cretaceous to Paleogene carbonates. Earth Sci. Rev. 96, 296–312.
Leprêtre, R., Barbarand, J., Missenard, Y., Gautheron, C., Pinna-Jamme, R., Saddiqi, O., 2017. Mesozoic evolution of NW Africa: implications for the Central Atlantic Ocean dynamics. J. Geol. Soc. 174 (5), 817–835. http://dx.doi.org/10.1144/jgs2016-100.
Lin, C., Bailey, S.W., 1985. Structural data for sudoite. Clay Clay Miner. 33, 410–414.
Marinčić, S., 1997. Tectonic structure of the island of Hvar (southern Croatia). Geologia Croatica 50 (1), 57–77.
Marynowski, L., Pisarzowska, A., Derkowski, A., Rakociński, M., Szaniawski, R., Środoń, J., Cohen, A.S., 2017. Influence of palaeoweathering on trace metal concentrations and environmental proxies in black shales. Palaeogeogr. Palaeoclimatol. Palaeoecol. 472, 177–191.
Mikes, T., Christ, D., Petri, D., Dunkl, I., Frei, D., Báldi-Beke, M., Reitner, J., Wemmer, K., Hrvatović, H., von Eynatten, H., 2008. Provenance of the Bosnian Flysch. Swiss J. Geosci. 101 (Supplement 1), 31–54. http://dx.doi.org/10.1007/s00015-008-1291-z.
Moore, D.M., Reynolds, R.C., 1997. X-ray Diffraction and the Identification and Analysis of Clay Minerals. Oxford University Press, Oxford–New York (378 pp.).
Pamić, J., 2002. The Sava–Vardar Zone of the Dinarides and Hellenides versus the Vardar Ocean. Eclogae Geol. Helv. 95, 99–113.
Papeš, J., Marinković, R., Raić, V., Magaš, N., Sikirica, V., 1982. Osnovna geološka karta SFRJ 1:100000. List Sinj K33–10 (Basic Geological Map of SFRJ 1:100000. Sinj Sheet). Geoinženjering Institut za geologiju Sarajevo, Geološki zavod OOUR za geologiju i paleontologiju Zagreb, Savezni geološki zavod, Beograd.
Ramovš, A., Hinterlechner-Ravnik, A., Kalenić, M., Karamata, S., Kochansky-Devidé, V., Mirković, M., Petkovski, P., Sremac, J., Krstić, B., Kulenović, E., Temkova, V., 1990. Stratigraphic correlation forms of Yugoslav Paleozoic. Rend. Soc. Geol. Ital. 12, 359–383.
Reiners, P.W., 2005. Zircon (U–Th)/He thermochronometry. In: Reiners, P.W., Ehlers, T.A. (Eds.), Low-temperature Thermochronology: Techniques, Interpretations, and Applications: Reviews in Mineralogy and Geochemistry. 58. pp. 151–176.
Reiners, P.W., Brandon, M.T., 2006. Using thermochronology to understand orogenic erosion. Annu. Rev. Earth Planet. Sci. 34, 419–466. http://dx.doi.org/10.1146/annurev.earth.34.031405.125202.
Reiners, P.W., Spell, T.L., Nicolescu, S., Zanetti, K.A., 2004. Zircon (U–Th)/He thermochronometry: He diffusion and comparisons with $^{40}Ar/^{39}Ar$ dating. Geochim. Cosmochim. Acta 68, 1857–1887.
Schmid, S.M., Bernoulli, D., Fügenschuh, B., Maţenco, L., Schefer, S., Schuster, R., Tischler, M., Ustaszewski, K., 2008. The Alpine–Carpathian–Dinaridic orogenic system: correlation and evolution of tectonic units. Swiss J. Geosci. 101, 139–183.
Scotese, C.R., 2002. http://www.scotese.com (PALEOMAP website).
Shuster, D., Farley, K.A., 2009. The influence of artificial radiation damage and thermal annealing on helium diffusion kinetics in apatite. Geochim. Cosmochim. Acta 73, 183–196.
Shuster, D., Flowers, R., Farley, K.A., 2006. The influence of natural radiation damage on helium diffusion kinetics in apatite. Earth Planet. Sci. Lett. 249, 148–161.
Sokač, B., Nikler, L., Velić, I., Mamužić, P., 1974. Osnovna geološka karta SFRJ 1:100000. List Gospić K33–127 (Basic Geological Map of SFRJ 1:100000. Gospić Sheet). Institut za geološka istraživanja Zagreb, Savezni geološki zavod, Beograd.
Sokač, B., Šćavničar, B., Velić, I., 1976a. Osnovna geološka karta SFRJ 1:100000. Tumač za list Gospić K33–127 (Basic Geological Map of SFRJ 1:100000. Geology of the Gospić Sheet). Institut za geološka istraživanja Zagreb, Savezni geološki zavod, Beograd, pp. 1–64.
Sokač, B., Šušnjar, M., Bukovac, J., Bahun, S., 1976b. Osnovna geološka karta SFRJ 1:100000. Tumač za list Udbina L33–128 (Basic Geological Map of SFRJ 1:100000. Geology of the Udbina Sheet). Institut za geološka istraživanja Zagreb, Savezni geološki zavod, Beograd, pp. 1–62.
Sremac, J., 2012. Influence of terrestrial sedimentation in Pennsylvanian rocks of Croatia. Geologia Croatica 65 (3), 273–282.
Środoń, J., 1976. Mixed-layer smectite/illites in the bentonites and tonsteins of the Upper Silesian Coal Basin. Pr. Mineral. 49 (84 pp.).
Środoń, J., 1984. X-ray powder diffraction identification of illitic materials. Clay Clay Miner. 32, 337–349.
Środoń, J., 2007. Illitization of smectite and history of sedimentary basins. In: Proceedings of the 11th EUROCLAY Conference, Aveiro, Portugal, pp. 74–82.
Środoń, J., Eberl, D.D., Drits, V.A., 2000. Evolution of fundamental-particle size during illitization of smectite and implications for reaction mechanism. Clay Clay Miner. 48, 446–458.
Środoń, J., Clauer, N., Eberl, D.D., 2002. Interpretation of K–Ar dates of illitic clays from sedimentary rocks aided by modelling. Am. Mineral. 87, 1528–1535.
Środoń, J., Kotarba, M., Biroň, A., Such, P., Clauer, N., Wójtowicz, A., 2006a. Diagenetic history of the Podhale–Orava basin and the underlying Tatra sedimentary structural units (western Carpathians): evidence from XRD and K–Ar of illite–smectite. Clay Miner. 41, 747–770.
Środoń, J., Clauer, N., Banaś, M., Wójtowicz, A., 2006b. K–Ar evidence for a Mesozoic thermal event superimposed on burial diagenesis of the Upper Silesia Coal Basin. Clay Miner. 41, 671–692.
Środoń, J., Zeelmaekers, E., Derkowski, A., 2009a. The charge of component layers of illite–smectite in bentonites and the nature of end-member illite. Clay Clay Miner. 57, 649–671.
Środoń, J., Clauer, N., Huff, W., Dudek, T., Banaś, M., 2009b. K–Ar dating of Ordovician bentonites from the Baltic Basin and the Baltic Shield: implications for the role of temperature and time in the illitization of smectite. Clay Miner. 44, 361–387.
Środoń, J., Paszkowski, M., Drygant, D.M., Anczkiewicz, A.A., Banaś, M., 2013. Thermal history of the Silurian in the Podolia segment of the SW margin of the East European Craton inferred from combined XRD, K–Ar, and AFT data. Clay Clay Miner. 61, 107–132.
Środoń, J., Szulc, J., Anczkiewicz, A., Jewuła, K., Banaś, M., Marynowski, L., 2014. Weathering, sedimentary, and diagenetic controls of mineral and geochemical characteristics of the vertebrate-bearing Silesian Keuper. Clay Miner. 49, 569–594.
Surić, M., Korbar, T., Juračić, M., 2014. Tectonic constraints on the late Pleistocene–Holocene relative sea-level change along the north-eastern Adriatic coast (Croatia). Geomorphology 220, 93–103.
Šušnjar, M., Sokač, B., Bahun, S., Bukovac, J., Nikler, L., Ivanović, A., 1973. Osnovna geološka karta SFRJ 1:100000. List Udbina L33–128 (Basic Geological Map of SFRJ 1:100000. Udbina Sheet). Institut za geološka istraživanja Zagreb, Savezni geološki zavod, Beograd.
Tari, V., 2002. Evolution of the northern and western Dinarides: a tectonographic approach. In: EGU Stephan Mueller Special Publication Series 1. pp. 223–236.
Tari-Kovačić, V., Mrinjek, E., 1994. The role of Palaeogene Clastics in the tectonic interpretation of northern Dalmatia (southern Croatia). Geologia Croatica 47, 127–138.
Tomljenović, B., Balling, P., Matoš, B., Vlahović, I., Herak, M., Herak, D., Blažok, L., Posarić, D., Širol, A., Schmid, S., Ustaszewski, K., 2017. Kinematic analysis of outcrop-scale joint and fault systems in the Mt. Velebit – implication to tectogenesis and active seismo-tectonics. In: 5th Reg. Mtg. Quaternary Geology Dedicated to Geohazards & Final Conf. LoLADRIA Project. Croatian Academy of Sciences and Arts, pp. 69–70.
Ustaszewski, K., Schmid, S.M., Fügenschuh, B., Tischler, M., Kissling, E., Spakman, W., 2008. A map-view restoration of the Alpine–Carpathian–Dinaridic system for the Early Miocene. Swiss J. Geosci. 101, S273–S294. http://dx.doi.org/10.1007/s00015-008-1288-7.
Ustaszewski, K., Schmid, S.M., Lugović, B., Schuster, R., Schaltegger, U., Bernoulli, D., Hottinger, L., Kounov, A., Fügenschuh, B., Schefer, S., 2009. Late Cretaceous intra-oceanic magmatism in the internal Dinarides (northern Bosnia and Herzegovina):

implications for the collision of the Adriatic and European plates. Lithos 108, 106–125.

Ustaszewski, K., Kounov, A., Schmid, S.M., Schaltegger, U., Krenn, E., Frank, W., Fügenschuh, B., 2010. Evolution of the Adria–Europe plate boundary in the northern Dinarides: from continent–continent collision to back-arc extension. Tectonics 29, TC6017. http://dx.doi.org/10.1029/2010TC002668.

Ustaszewski, K., Herak, M., Tomljenović, B., Herak, D., Matej, S., 2014. Neotectonics of the Dinarides–Pannonian Basin transition and possible earthquake sources in the Banja Luka epicentral area. J. Geodyn. 82, 52–68.

Vlahović, I., Tišljar, J., Velić, I., Matičec, D., 2005. Evolution of the Adriatic Carbonate Platform: Palaeogeography, main events and depositional dynamics. Palaeogeogr. Palaeoclimatol. Palaeoecol. 220, 333–360. http://dx.doi.org/10.1016/j.palaeo.2005.01.011.

Vlahović, I., Mandic, O., Mrinjek, E., Bergant, S., Ćosović, V., De Leeuw, A., Enos, Paul, Hrvatović, H., Matičec, D., Mikša, G., Nemec, W., Pavelić, D., Penciger, V., Velić, I., Vranjković, A., 2012. Marine to continental depositional systems of Outer Dinarides foreland and intra-montane basins (Eocene–Miocene, Croatia and Bosnia and Herzegovina). Field Trip Guide, 29th IAS Meeting of Sedimentology, Schladming/Austria. J. Alpine Geol. 54, 405–470.

Wagner, G., Van den Haute, P., 1992. Fission-track Dating. Kluwer Acad, Dordrecht (285 pp.).

Weber, J., Vrabec, M., Pavlovcic-Preseren, P., Dixon, T., Jiang, Y., Stopar, B., 2010. GPS-derived motion of the Adriatic microplate from Istria Peninsula and Po Plain sites, and geodynamic implications. Tectonophysics 483, 214–222.

Werner, T., Lewandowski, M., Vlahović, I., Velić, I., Sidorczuk, M., 2015. Palaeomagnetism and rock magnetism of the Permian redbeds from the Velebit Mt. (Karst Dinarides, Croatia): dating of the early Alpine tectonics in the western Dinarides by a secondary magnetization. Tectonophysics 651–652, 199–215.

Wilson, M.J., 2013. Sheet Silicates: Clay Minerals. The Geological Society, London (724 pp.).